This is the peer-reviewed, final accepted version for American Mineralogist, published by the Mineralogical Society of America.
The published version is subject to change. Cite as Authors (Year) Title. American Mineralogist, in press.
DOI: https://doi.org/10.2138/am-2023-9153. http://www.minsocam.org/

**Revision 1**

# Solfataric Alteration at the South Sulfur Bank, Kilauea, Hawaii, as a Mechanism for Formation of Sulfates, Phyllosilicates, and Silica on Mars

Janice L. Bishop[1], Peter Schiffman[2], Enver Murad[3], Randal J. Southard[4], Lukas Gruendler[1], M. Darby Dyar[5-6], and Melissa D. Lane[7]

[1]SETI Institute, Mountain View, CA, 94043 (jbishop@seti.org).

[2]Dept. of Geology, Univ. of Calif., Davis, CA, 95616.

[3]Bavarian Geologic Survey, Marktredwitz, Germany.

[4]Dept. of Land, Air and Water Resources, Univ. of Calif., Davis, CA, 95616.

[5]Planetary Science Institute, Tucson, AZ, 85719.

[6]Mount Holyoke College, South Hadley, MA, 01075.

[7]Fibernetics, Lititz PA 17543.

Note: co-author E. Murad has unfortunately passed since we started work on this paper.

Keywords:

Kilauea, hydrothermal, solfataric alteration, sulfates, smectites, reflectance spectroscopy, Mars

*Submitted to American Mineralogist, August 11, 2023*

*Revised April 2, 2024*

**Abstract**

Solfataric alteration at the South Sulfur Bank of the former Kilauea caldera produced opal, Mg- and Fe-rich smectites, gypsum, and jarosite through silica replacement of pyroclastic Keanakako'i ash and leaching of basaltic lavas. This site on the island of Hawaii serves as an analog for formation of several minerals found in altered deposits on Mars. Two distinct alteration environments were characterized in this study including a light-toned, high-silica, friable outcrop adjacent to the vents, and a bedded outcrop containing alternating orange/tan layers composed of smectite, gypsum, jarosite, hydrated silica, and poorly crystalline ferric oxide phases. This banded unit likely represents deposition of pyroclastic material with variations in chemistry over time that was subsequently altered via moderate hydrothermal and pedogenic processes and leaching of basaltic caprock to enhance the Si, Al, Mg, Fe, and Ca in the altered layers. In the light-toned, friable materials closest to the vents along the base of the outcrop glassy fragments were extensively altered to opal-A plus anatase.

Lab measurements of samples returned from the field were conducted to replicate recent instruments at Mars and provide further characterization of the samples. These include elemental analyses, sample texture, XRD, SEM, VNIR/mid-IR reflectance spectroscopy, TIR emittance spectroscopy, and Mössbauer spectroscopy. Variations in the chemistry and mineralogy of these samples are consistent with alteration through hydrothermal processes as well as brines that may have formed through rain interacting with sulfuric fumes. Silica is present in all altered samples and the friable pyroclastic ash material with the strongest alteration contains up to 80 wt.% $SiO_2$.

Sulfate mineralization occurred at the South Sulfur Bank through fumarolic action from vents and likely included solfataric alteration from sulfuric gases and steam, as well as oxidation of sulfides in the basaltic caprock. Gypsum and jarosite are typically present in different layers of the altered wall, likely because they require different cations and pH regimes. The presence of both jarosite and gypsum in some samples implies high sulfate concentrations and the availability of both $Ca^{2+}$ and $Fe^{3+}$ cations in a brine percolating through the altered ash. Pedogenic conditions are more consistent with the observed Mg-smectites and gypsum in the tan layers, while jarosite and nontronite likely formed under more acidic conditions in the darker orange layers. Assemblages of smectite, Ca-sulfates, and jarosite similar to the banded orange/tan unit in our study are observed on Mars at Gale crater, Noctis Labyrinthus, and Mawrth Vallis, while high-silica outcrops have been identified in parts of Gusev crater, Gale crater, and Nili Patera on Mars.

## Introduction

The surface of Mars is shaped by volcanism and impacts, many of which created hydrothermal environments and sulfate brine alteration. The minerals formed under hydrothermal conditions or through sulfate brine activity on Mars can help us trace back the ancient geochemical history of surface and near-surface environments. Investigating terrestrial hydrothermal environments provides geochemical context for better understanding martian processes that may have supported warmer settings with liquid water and habitable conditions (e.g., Walter and Des Marais 1993; Schulze-Makuch et al. 2007; Black and Hynek 2018) on an otherwise arid and cold planet. Evidence collected by the Mars Exploration Rover (MER) Spirit suggests the actions of hydrothermal processes contributed to the unusual sulfates at Paso Robles class outcrops (Johnson et al. 2007; Lane et al. 2008; Yen et al. 2008; Parente et al. 2009) and the high silica environments at Home Plate (Squyres et al. 2007; Ruff et al. 2011; Ruff and Farmer 2016). Numerous outcrops of sulfates in the greater Valles Marineris region are products of sulfate brines, especially where gypsum and jarosite are observed (Bishop et al. 2009; Murchie et al. 2009; Roach et al. 2010; Weitz et al. 2011; Thollot et al. 2012; Bishop et al. 2021a). Smaller patches of Ca sulfates and jarosite/alunite are associated with phyllosilicates at Mawrth Vallis (Bishop et al. 2020; 2023), Noctis Labyrinthus (Weitz et al. 2011; 2013), and Cross crater (Ehlmann et al. 2016), indicating alteration with sulfate brines or hydrothermal processes.

Burns (1988; 1993) proposed clay-sulfate-iron oxide/oxyhydroxide assemblages on the surface of Mars that could be derived from aqueous alteration of volatile- and iron-rich basaltic rocks containing fayalitic olivine, iron-rich pyroxenes, and accessory sulfides. Burns (1988) emphasized the importance of these materials for understanding martian geochemistry by paraphrasing Jensen and Bateman (1979): *These minerals "arrest attention and incite interest as to what they may mask ….The finding of one may herald the discovery of buried wealth."* Acidic groundwater was proposed to react with igneous silicate minerals and iron sulfides to yield jarosite, alunite, and other minerals (Burns 1987; Burns and Fisher 1993). Iron sulfides and igneous silicate minerals are plentiful in martian meteorites (e.g., Bunch and Reid 1975; McSween 1994; McCubbin et al. 2009) and have been inferred as martian surface components since Vikings' measurements (e.g., Toulmin et al. 1977; Clark and Baird 1979; McSween 2002), and dissolved volcanic gases on Mars would have produced acidic groundwaters (Gooding 1978). More recently, Moore & Szynkiewicz (2023) built upon this idea to describe a sulfur cycle whereby volcanism contributes sulfur to the

63 groundwater and low-temperature chemical alteration produces sulfates in aqueous surface
64 environments.

65 Elwood Madden et al. (2004; 2009; 2012) extended this early work by Burns through modeling
66 the conditions supporting formation of jarosite. These studies support formation of jarosite
67 together with iron oxides/hydroxides and clays on Mars as predicted by Burns (1988). Black &
68 Hynek (2018) summarize a host of sulfates including jarosite and gypsum that form together with
69 phyllosilicates and iron oxides/hydroxides in terrestrial analog environments. Recent brine
70 experiments demonstrate that gypsum forms readily through the action of sulfate brines on
71 smectites (Geyer et al. 2023). Coordinating field observations with lab investigations using
72 instruments at Mars furthers our ability to connect the geochemical environments governing
73 mineral formation with specific sites on Mars. Trace amounts of jarosite are observed in the
74 Murray formation along the lower region of Mount Sharp in Gale crater (Rampe et al. 2020), while
75 gypsum and Ca sulfates (anhydrite, bassanite, gypsum) are more commonly observed at higher
76 elevations on Mount Sharp (Vaniman et al. 2018). CheMin XRD analyses of the lacustrine
77 Marimba and Sebina samples indicate combinations of jarosite, gypsum, smectite, and amorphous
78 phases (Achilles et al. 2020). Marimba contains 1.7 wt.% jarosite, 3.5 wt.% gypsum, 19 wt.%
79 smectite, and ~50 wt.% amorphous phases, while Sebina includes 2.5 wt.% jarosite, 6.6 wt.%
80 gypsum, 28 wt.% smectite, and ~40 wt.% amorphous phases (Achilles et al. 2020).

81 Solfataric alteration of basalts and volcanic ash may have played a role in sulfate mineralization
82 on Mars through fumarolic action from vents (e.g., Morris et al. 2000; Schiffman et al. 2006;
83 Bishop et al. 2007). Solfataric processes are defined here as alteration through fumarolic activity
84 and/or "acid-fog" deposition occurring as the sulfuric fumes emanating from vents react with the
85 ash and tephra (Schiffman et al., 2006). Solfataric alteration promotes silicification of basalt and
86 also the formation of sulfates, amorphous silica, and layer silicates, resulting in partial
87 consolidation of ash/tephra particles and/or crust formation on ash surfaces (Schiffman et al.,
88 2006). Fumaroles in the Kilauea caldera, HI, have created a solfataric bank on the south wall of
89 the crater through alteration of the Keanakako'i ash that was previously deposited there. This study
90 focuses on field observations of the "South Sulfur Bank" Kilauea solfatara site, lab measurements
91 of samples collected there, and implications for hydrothermal alteration and the action of sulfate
92 brines at solfatara sites on Mars.

93

## Field Site

### Location of study site

The solfatara site studied here was located in a light-toned pyroclastic ash bed underneath the 1982 flow along the southern rim of Kilauea caldera at an elevation of 1104 m at 19°24'12.9"N and 155°16'28.7"W (Figure 1). Lava flows in 1974 and 1982 near the Kilauea caldera are dominated by Pahoehoe lava and extend southwest to Mauna Iki and southeast to Mauna Ulu. These flows are rich in olivine and calcic feldspar and typically contain only small amounts of pyroxene (Wolfe and Morris 1996).

### Character of study site

Our study site was termed South Sulfur Bank to differentiate it from the Sulfur Banks site at the north side of Kilauea inside Hawaii Volcanoes National Park. Both sites contain vents exuding sulfuric gases. The South Sulfur Bank outcrop formed east of the Halema'uma'u crater and west of the Keanakako'i crater and was part of the Keanakako'i Ash Member from the 1790 flow (Figure 2). The solfatara outcrop was composed of thin layers of basaltic pumice and was present in some localities as 10-m thick pyroclastic deposits (Wolfe and Morris 1996; Schiffman et al. 2000). The sequence contained bedded vitric ash with cross-bedded deposits of lapilli and blocks that were coarser than the ash. At the base of the solfatara outcrop several small vents were present that periodically exhibited wisps of gases and/or steam. The Halema'uma'u crater became active again in 2008, forming a lava lake and steam. In 2018 seismic activity increased, fissures formed, and the wall southeast of Halema'uma'u crater containing this South Sulfur Bank site collapsed (https://www.usgs.gov/volcanoes/kilauea/2018-lower-east-rift-zone-eruption-and-summit-collapse; latest revision Nov. 24, 2023).

Members of our team visited the site in 2003, 2004, and 2006 with assistance from the Hawaiian Volcanoes National Park (HAVO) staff and permits issued to Schiffman (2003) and Bishop (2004, 2006). We accessed the site by hiking northeast across the 1982 flow from the rim road down towards the caldera. Our study site focused on the thick pyroclastic deposit of the South Sulfur Bank site (Figure 2-3). Alteration of the basaltic flow above the South Sulfur Bank produced orange- to tan-colored fine-particulate material that seeped downhill in some places and pigmented portions of the solfatara unit (Figure 2e, 3a).

This is the peer-reviewed, final accepted version for American Mineralogist, published by the Mineralogical Society of America.
The published version is subject to change. Cite as Authors (Year) Title. American Mineralogist, in press.
DOI: https://doi.org/10.2138/am-2023-9153. http://www.minsocam.org/

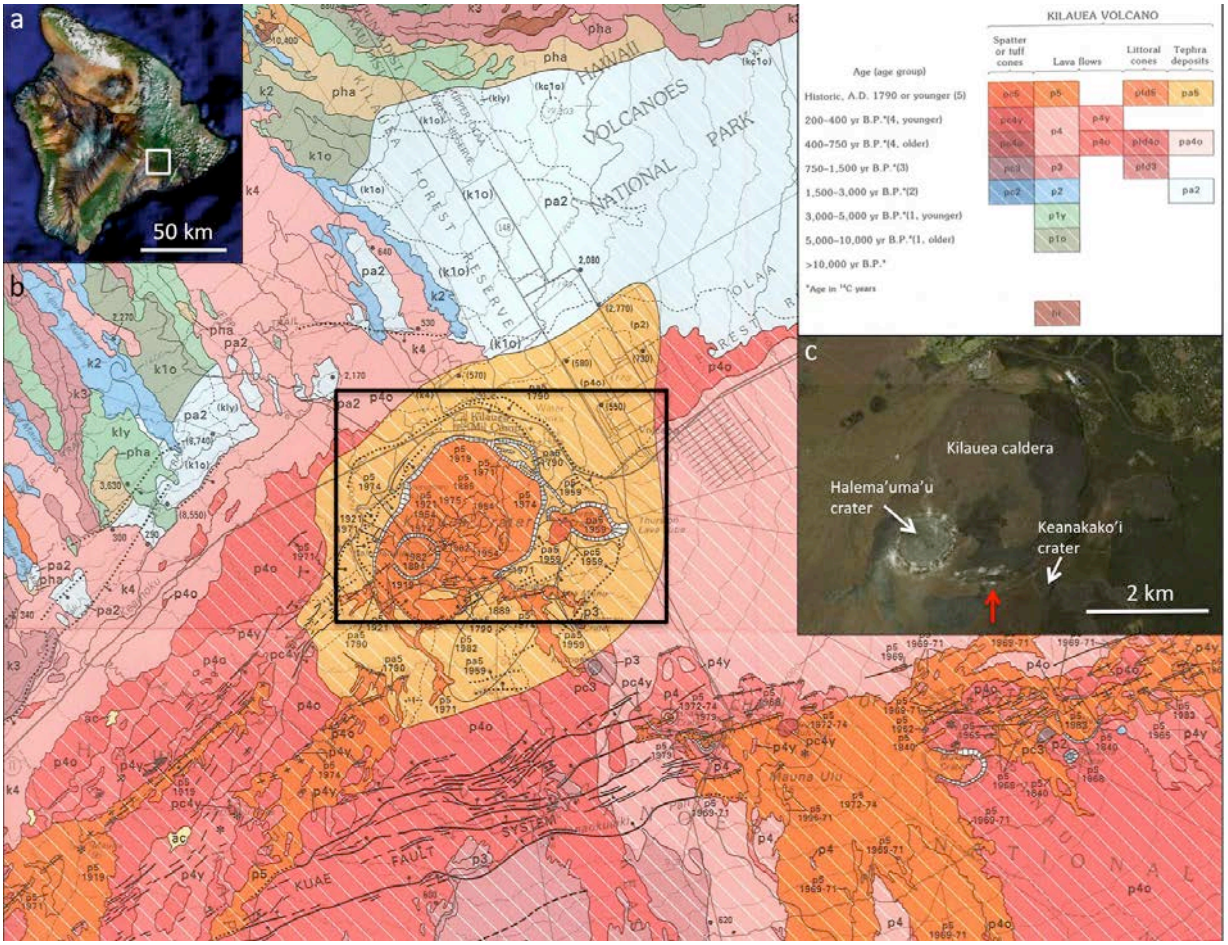


**Figure 1 Location of study site at Kilauea, HI.** a) View of the island of Hawaii (credit: Digital Globe, Google Earth view retrieved 07/11/2008) with the region in b labeled by a white box, b) Portion of volcanic flow map (Wolfe and Morris, 1996) with a black box indicating the site of c, and c) View of the Kilauea caldera with the solfatara site marked by a red arrow (credit: Digital Globe, Google Earth view retrieved 07/11/2008).

The solfatara outcrop is composed of orange/tan-colored altered material below the brown basalt and wide expanses of white/beige material extending for ~20 meters at the thickest location with a height of ~3 meters. The brownish-orange altered basalt from the 1974 flow above our field site was investigated recently and contains silica, iron oxides, and sulfates in addition to basalt (Yant et al., 2018). The black 1982 flow covered the 1974 flow (altered to brownish color) above our field site and at the base of the field site including portions of the white/beige material. A slight smell of sulfur at the site was noted at each visit to the site (2003, 2004, 2006) near several small weakly active hydrothermal vents in the direction of the floor of the Halema'uma'u crater. Thin

columns of steam and/or gases emanated periodically from a few small vents consistent with low activity levels in the caldera.

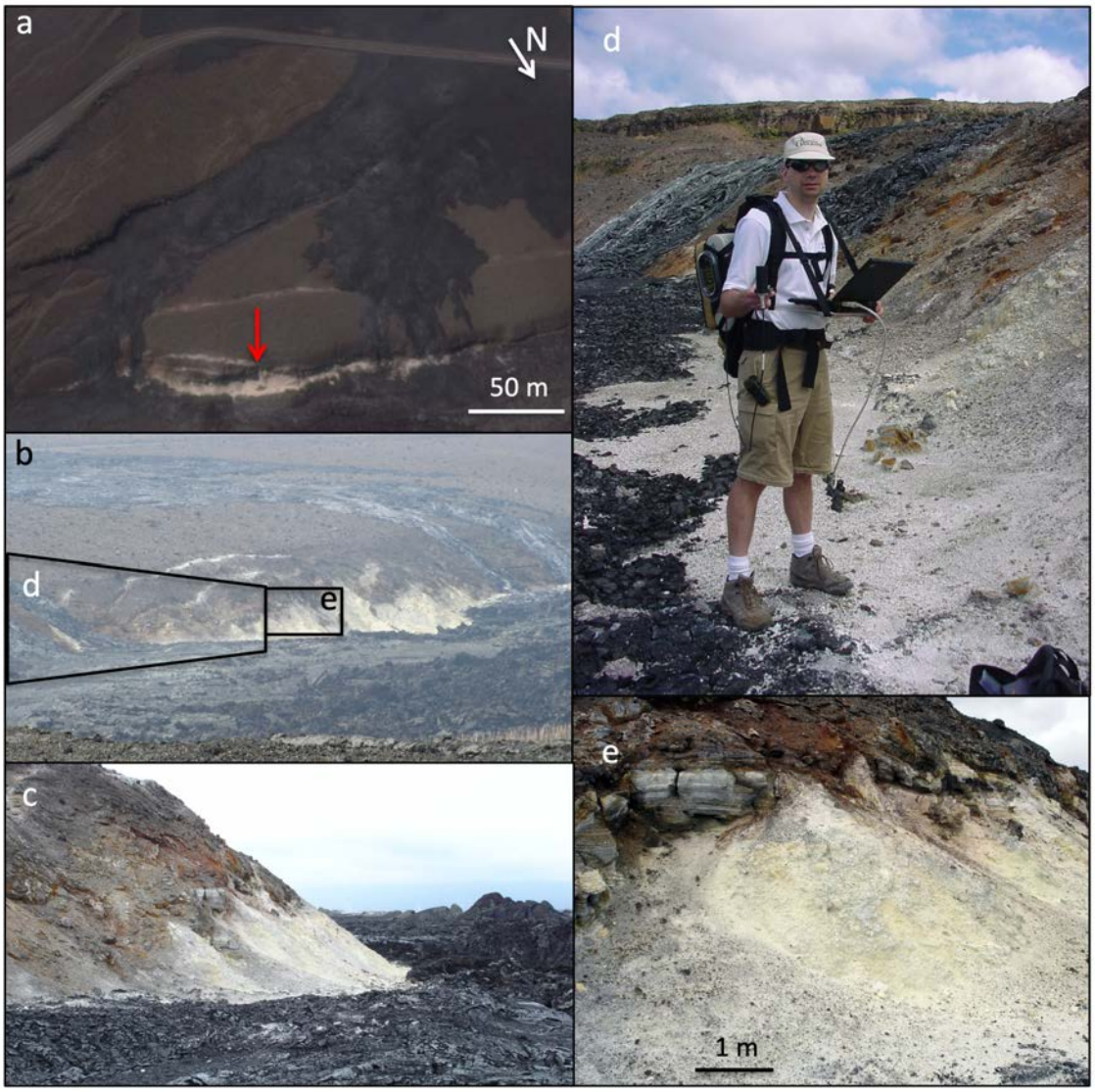


**Figure 2 Location of the solfatara outcrop along the southern rim of the Kilauea caldera.** a) View of 1982 flow covering Keanakako'i Ash Member with red arrow marking field site (credit: Digital Globe, Google Earth view retrieved 02/02/2007), b) Photo of site taken in 2006 from the rim road across the Kilauea caldera with locations marked for panels d and e, c) Ash bed covered and surrounded by 1974 and 1982 lava flows along the floor of the caldera (photo from 2006; height of light-toned ash exposure ~5 meters), d) LG in 2004 with field spectrometer showing altered ash outcrop on right, brownish alteration from the 1974 lava, and the black/gray 1982 flow in the background, and e) Altered, bedded outcrops below the basaltic caprock, and friable altered ash ranging in color from white to yellow to beige (photo from 2006).

This is the peer-reviewed, final accepted version for American Mineralogist, published by the Mineralogical Society of America.
The published version is subject to change. Cite as Authors (Year) Title. American Mineralogist, in press.
DOI: https://doi.org/10.2138/am-2023-9153. http://www.minsocam.org/

# Methods

## Samples

Samples were collected from the bedded pyroclastic deposit and the powdery friable deposit of the South Sulfur Bank site during three field seasons in 2003, 2004, and 2006 and are summarized in Table 1. The locations of these samples are shown in Figure 3. Layers of alternating white/light and orange/gray material were collected in 2003 (Figure 3a) to investigate changes in chemistry and mineralogy of the layers. An ASD FieldSpecPro spectrometer (described below) was used at the field site in 2004 and 2006 to select samples from the layered pyroclastic deposits (tan/gray/orange materials), as well as the white/beige friable unit. These additional materials were collected in 2004 and 2006 to characterize the altered solfatara from multiple regions of the outcrop.

**Table 1. Description of Solfatara Samples from South Sulfur Bank inside Kilauea Caldera**

| Sample Category | Sample ID | Collection Date | XRD Minerals | Description and Notes |
|---|---|---|---|---|
| Type 1 | JB629 | 2003 | opal<br>anatase | PS# 9120301-A, white/beige friable material adjacent to layered outcrop |
| | JB632 | 2004 | opal<br>anatase<br>cristobalite, tr<br>tridymite, tr | white/beige friable material ~2 meters to the right of layered outcrop |
| | JB776 | 2006 | opal<br>anatase<br>quartz, tr<br>feldspar, tr | white/beige/yellow friable material ~1 meter to right of JB632 |
| Type 2 | JB630 | 2003 | | PS# 9120301-B, layered outcrop, orange material |
| | JB633 | 2004 | gypsum<br>jarosite<br>Mg-smectite<br>nontronite | layered outcrop, thick orange unit (insufficient material for chemical analyses) |
| | JB643 | 2004 | | portions of sample JB633 crushed again and re-sieved <45 μm |
| | JB777 | 2006 | gypsum<br>jarosite<br>Mg-smectite<br>Nontronite | layered outcrop, thick orange unit ~10 cm to the right of JB633 (surface eroded, site of JB633 no longer visible) |

| | | | | | |
|---|---|---|---|---|---|
| Type 3 | JB631 | 2003 | | PS# 9120301-C, layered outcrop, gray and orange material |
| Type 4 | JB775 | 2006 | sulfur | base of slump of friable material yellow crumbles from white and yellow rock |

Notes: Major minerals identified by XRD listed where run; tr indicates trace amounts.

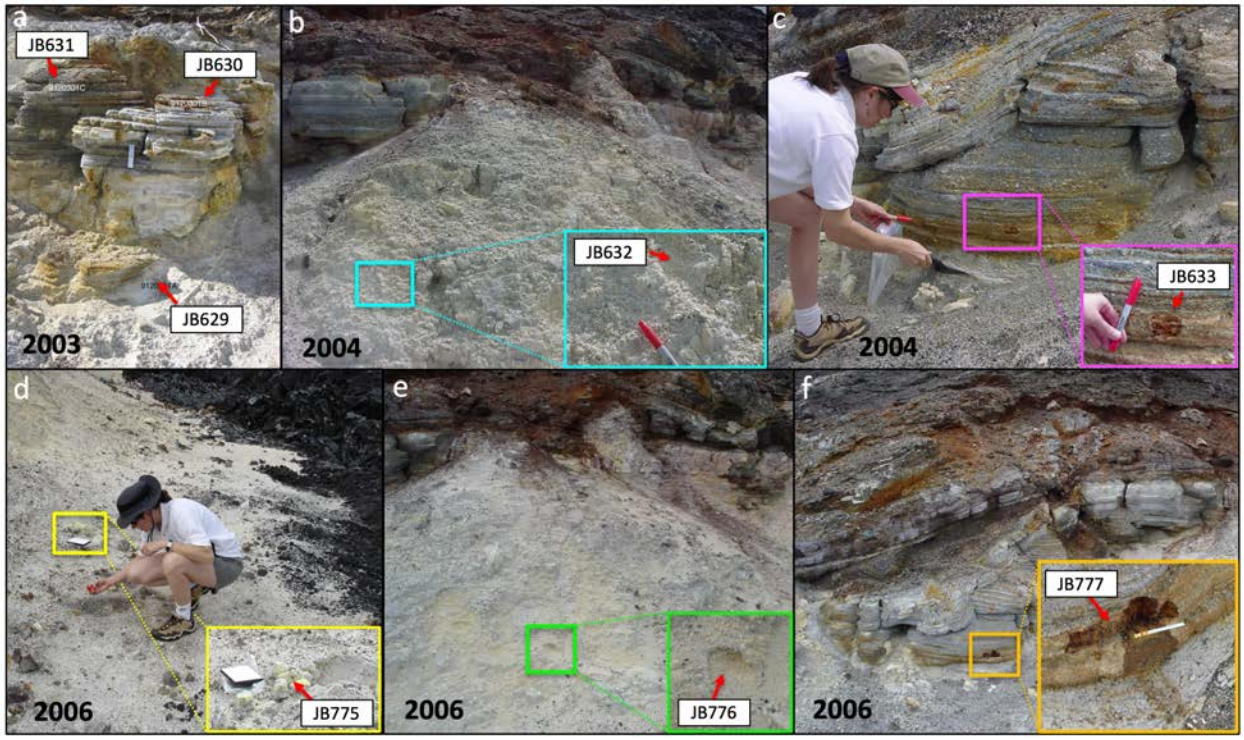


**Figure 3. Sample Collection Sites.** a) Samples collected by PS in 2003 from banded orange/white ash units and friable white/yellow material. b) Sample of friable white/yellow material collected in 2004 by JLB and LG with expanded view in turquoise box. c) Sample of orange banded crust material collected in 2004 by JLB and LG with expanded view of orange layers in pink box. d) White rocks containing consolidated silica/ash with yellow native S underneath, collected in 2006 by JLB, with expanded view in yellow box. e) Sample of friable white/yellow material collected in 2006 by JLB (similar to 2004 sample but different location) with expanded view in green box. f) Sample of orange banded crust material collected in 2006 by JLB (from same orange unit as 2004 sample, but outer surface was eroded) with expanded view in orange box.

## Visible-near infrared (VNIR) reflectance spectra of whole samples

VNIR reflectance spectra were acquired both in the field and in the lab using an Analytical Spectral Devices (ASD) FieldSpecPro spectrometer with Spectralon as the white standard. Spectral sampling is 1.4 nm from 0.35 to 1.05 μm and 2 nm from 1.05 to 2.5 μm with a spectral resolution of 3 nm in the visible region and 10 nm in the near-infrared (NIR) region. Spectra were

measured in the field using the 1° optics and the contact probe. The contact probe configuration collects spectra for a circular region ~1 cm in diameter and provided sufficiently clean spectra for mineral identification in the field. Additional spectra were measured in the lab of samples from multiple sites along the surface of whole rock samples in order to guide sampling of the rocks for further analyses.

**Thermal infrared (TIR) emissivity spectra**

Emission spectra were measured of rock samples at the Mars Space Flight Facility at Arizona State University (ASU) using a Nicolet Nexus 670 E.S.P. FT-IR interferometric spectrometer, as in previous studies (Christensen et al. 2000). This spectrometer was modified for emission measurements and used a thermoelectrically stabilized DTGS detector and a CsI beam splitter for measurement of emitted radiation over the mid-infrared range of 4000 to 200 $cm^{-1}$ where thermal infrared (TIR) provides a strong signal for rocks and coarse-grained samples (Lane and Bishop 2019).

**Preparation of particulate samples**

The soil and rock samples were divided by color and spectral properties and gently crushed and dry sieved to <125 μm for further study in the lab. These particulate materials were used for elemental analyses, XRD, SEM, Mössbauer spectroscopy, and additional reflectance spectroscopy measurements at the Reflectance Experiment Laboratory (RELAB) at Brown University.

**Bulk major element chemistry**

Samples with sufficient material were sent to the Bureau Veritas labs (https://www.bvna.com/) for X-ray Fluorescence (XRF) determination of the major elements as oxides. Total C, total S, and sulfate abundance were also determined using a LECO elemental analyzer. These include JB629, JB631, JB632, JB775, JB776, and JB777. Lost on ignition (LOI) values were determined by heating to 1000 °C.

**Microprobe analyses**

Wavelength dispersive scanning electron microprobe (SEM) analyses were performed on epoxide-impregnated, polished sections or particles smear-mounted on double-sided sticky carbon

tape coated with carbon for samples JB629, JB630, and JB631 at UC Davis as in previous studies (Schiffman et al. 2000; Bishop et al. 2002; Schiffman et al. 2002; 2006). Back-scattered electron (BSE) images were acquired and evaluated for petrographic features and degree of consolidation of the textures. Quantitative, wavelength dispersive analyses by electron microprobe analysis (EMPA) were conducted using a Cameca SX-100 microprobe operated at 15 KeV, 5 or 10 nÅ beam current, and variable spot size in order to map out changes in elemental composition across the samples.

**XRD**

X-ray diffraction (XRD) analyses were performed at UC Davis on oriented aggregates of the particulate material from samples JB629, JB632, JB775, JB776, and JB777 mounted on glass slides with a Diano 8000 diffractometer (Cu Kα radiation) as in previous studies (Schiffman et al. 2002; 2006). Additional XRD analyses were performed on powdered aliquots of samples JB632 and JB633 at the Bavarian Geologic Survey using Cu Kα radiation on a Bruker D8 instrument equipped with a sample spinner and a diffracted-beam graphite monochromator as in previous studies (e.g., Murad and Rojik 2003; Bishop et al. 2004).

**Visible-infrared reflectance spectra of particulate samples**

VNIR to mid-IR reflectance spectra were measured for the particulate samples at RELAB as described in previous experiments (Bishop et al. 2007). Bidirectional VNIR spectra were measured relative to Halon under ambient conditions from 0.3 to 2.5 μm. Biconical reflectance spectra were measured from ~1 to 25 μm relative to a rough gold surface using a Nicolet 740 Fourier transform infrared interferometer (FTIR) in a $H_2O$- and $CO_2$-purged environment in order to remove adsorbed water from the samples. Composite, absolute reflectance spectra were prepared by scaling the FTIR data to the bidirectional data near 1.2 μm. The spectral resolution is 5 nm for the bidirectional data and 4 $cm^{-1}$ for the FTIR data.

**Mössbauer spectra of particulate samples**

Mössbauer measurements were taken at 295K, on a Web Research Co. W100 spectrometer on samples JB632 and JB633 mixed with sucrose using a ~10 mCi 57Co source in rhodium from -4 to +4 mm/s velocity. Run times ranged from 24-48 hours. Spectra were collected in 2048 channels

and then all spectral baselines were corrected for the Compton scattering of 122 keV gamma rays by electrons inside the detector. The corrected data are equal to A/(1-b), where A is the counts of the uncorrected absorption and b is the Compton fraction determined through recording the counts with and without a 14.4 keV stop filter (~2 mm Al foil) in the gamma ray beam. While this correction does not change the results of the fits, it does allow for accurate determination of the % absorption in each spectrum. Each spectrum was then folded and corrected for nonlinearity in WMOSS. Interpolation to a linear-velocity scale was accomplished using the room temperature spectrum of 25 μm α-Fe foil as a calibration standard.

The Mössbauer spectra were fit using the Dist3e program as in Dyar et al. (2008). The widths of quadrupole doublets or magnetic sextets were constrained to vary together, while doublets were constrained to have two equal peaks and sextets to have peaks in the ratio 3:2:1:1:2:3. Quadrupole splitting (QS) values of doublets and magnetic fields of sextets were varied over a range, and isomer shift (IS) values and peak widths were either fixed or left unconstrained. These IS and QS values can be used to identify or constrain the presence of Fe-bearing minerals in samples (Dyar and Sklute 2019).

## Results

### Geochemistry and mineralogy of samples

Elemental trends and XRD analyses for samples of the white/beige friable materials and the orange/tan bedded units were similar for samples collected on different field trips. Bulk elemental analyses are provided in Table 2 for samples with sufficient material (JB629, JB630, JB631, JB632, JB775, JB776, and JB777) and two samples were measured twice to check for consistency among different sample alliquots. The white/light samples (Type 1) include primarily $SiO_2$ (~74-81 wt.%), $TiO_2$ (3-11 wt.%), and $SO_3$ (0-2 wt.%) as sulfate and elemental S with additional minor/trace amounts of Al, Fe, Mg, Ca, and C (Table 1). These samples also include loss on ignition (LOI) values ranging from ~12-15 wt.% (includes C and S values) that are consistent with the presence of opal in these samples. The layered orange materials (Type 2) have lower $SiO_2$ (~44-51 wt.%) and $TiO_2$ (3-11 wt.%) levels and higher amounts of the major geologic elements, consistent with the altered portions of Keanakako'i_ash from Schiffman et al. (2000). The Type 3 gray and orange sample has lower $SiO_2$ (~42-43 wt.%) and higher MgO (10-13 wt.%) levels compared to the layered orange Type 2 samples and is more similar to the glassy grains of the

Keanakako'i_ash (Schiffman et al., 2000). Type 4 contains primarily elemental S with ~16 wt.% $SiO_2$.

Microprobe analyses of several regions of samples JB629, JB630, and JB631 are reported in Table S1 and average values for each type of composition are presented in Table 3 for comparison with the bulk chemistry for those samples. SEM analyses of ash and tephra from the Kilauea region show replacement of glass and formation of rinds in the ash material (Schiffman et al. 2000). Much of the material in the glassy grains and rinds in the friable white/light material (Type 1 samples JB629, JB632, JB776) was replaced by silica and the $SiO_2$ abundance is significantly elevated for these samples compared with that of the fresh glass and orange/tan samples JB630 and JB777 (Type 2), and JB631 (Type 3) (Tables 2-3). XRD shows these bright, friable samples to be primarily opal (Table 1, Figure 4), which is consistent with the ~80 wt.% $SiO_2$ observed. Microprobe analyses of an aliquot of sample JB629 displays these glassy grains and rinds that were replaced by silica (Figure 5a). A portion of sample JB629 containing yellow grains reveals the presence of native sulfur (Figure 5b). This is consistent with the ~66 wt.% S and ~16 wt.% $SiO_2$ for JB775 that is mostly yellow crumbles separated from the friable white/light material. XRD also identified anatase in samples JB629 and JB776, which is consistent with the elevated $TiO_2$ levels (Table 2). Limited C is observed in all samples (≤0.5 wt.%), constraining the amount of organics or carbonates that can be present (Table 2).

XRD measured gypsum, jarosite, saponite, and nontronite in the layered light gray and orange materials (Table 1, Figure 4). Microprobe analyses of Type 3 sample JB631 (Figure 5c) found glassy grains and rinds as for Type 1 JB629 (white/light) and Type 2 JB630 (layered orange) as well as smectite rich in Mg and Fe, and bright phases extremely high in Fe, and also high in S, P, and Al. These bright materials include jarosite, as well as poorly crystalline iron oxide phases not detected by XRD and likely also amorphous phases containing P. The abundance of these bright Fe-sulfate grains is much higher in the microprobe analyses of Type 3 sample JB631 enabling determination of their chemistry, including ~55-60% $Fe_2O_3$, ~7-12% $Al_2O_3$, ~12-13% $SO_3$ and ~3% $P_2O_5$. Elemental variations across these bright spots indicate nonlinear Fe/S correlations, indicating that S is present in other materials besides jarosite, or that some of the jarosite contains high Al levels, similar to alunite. Gypsum is also observed in selected Type 2 bedded orange materials through XRD (Figure 4), microprobe analyses (Figure 5), and VNIR reflectance spectra (Figure 6) and is likely present in the lighter-colored grains in these primarily orange/tan samples.

This is the peer-reviewed, final accepted version for American Mineralogist, published by the Mineralogical Society of America.
The published version is subject to change. Cite as Authors (Year) Title. American Mineralogist, in press.
DOI: https://doi.org/10.2138/am-2023-9153. http://www.minsocam.org/

Sample JB777 has elevated $SO_3$ levels and also higher $Fe_2O_3$ and CaO, consistent with Ca sulfates in addition to jarosite in that sample.

The XRD results for Type 2 orange layered samples JB633 and JB777 show stronger peaks consistent with saponite and hectorite than with nontronite (Figure 4), which is consistent with roughly three times more MgO than $FeO^T$. Interestingly, a combination of hectorite, saponite, and nontronite is needed to account for the smectite peaks in these samples. All three smectites include XRD peaks near 19.4-19.8, 34.5-35, and 53 °2Θ, while only saponite and nontronite have a peak near 5.7-6 °2Θ, only hectorite and nontronite have a peak near 29 °2Θ, and only saponite and hectorite have a peak near 61 °2Θ. Microprobe analyses of Mg-rich smectite in sample JB631 indicate 50.4% $SiO_2$, 17.3% $Al_2O_3$, 14.4% MgO, 4.5% $Fe_2O_3$ (as $Fe^{3+}$ and/or $Fe^{2+}$), 0.1% CaO, 0.9% MnO, 0.7% $P_2O_5$ and <0.1% of other oxides (Table 3, S1). Additionally, the glassy grains examined in microprobe analyses of JB630 and JB631 (Table 3, S1) contain ~13 wt.% $Al_2O_3$, ~11 wt.% $FeO^T$ (where the total Fe is expressed as FeO, but both $Fe^{2+}$ and $Fe^{3+}$ are likely present), ~8 wt.% MgO, and ~10 wt.% CaO that are almost entirely lost through alteration to form the altered glassy grains and rinds of JB629. Ti is present in nearly all of the samples and is likely present in the basaltic glass for the orange/gray layered samples (Table 1).

This is the peer-reviewed, final accepted version for American Mineralogist, published by the Mineralogical Society of America.
The published version is subject to change. Cite as Authors (Year) Title. American Mineralogist, in press.
DOI: https://doi.org/10.2138/am-2023-9153. http://www.minsocam.org/

**Table 2a** **Major elements in weight percent**

| Sample Type | Sample ID | $SiO_2$ wt.% | $Al_2O_3$ wt.% | $Fe_2O_3^T$ wt.% | MgO wt.% | CaO wt.% | $Na_2O$ wt.% | $K_2O$ wt.% | $TiO_2$ wt.% | LOI wt.% | Sum wt.% | $C_{tot}$ wt.% | $S_{tot}$ wt.% | $SO_3$ wt.% | $S_{sulfate}$ wt.% | $S_{elem}$ wt.% |
|---|---|---|---|---|---|---|---|---|---|---|---|---|---|---|---|---|
| Type 1 | JB629-1 | 80.6 | 0.3 | 0.7 | 0.0 | 0.0 | 0.0 | 0.0 | 3.6 | 14.6 | 100.0 | 0.1 | 0.8 | 0.0 | 0.0 | 0.8 |
| | JB629-2 | 80.5 | 0.4 | 0.8 | 0.1 | 0.1 | 0.0 | 0.0 | 3.4 | 14.7 | 100.0 | 0.5 | 1.1 | 1.3 | 0.5 | 0.6 |
| | JB632 | 73.8 | 0.5 | 0.8 | 0.2 | 0.1 | 0.0 | 0.0 | 10.5 | 13.8 | 100.0 | 0.1 | 3.1 | 1.8 | 0.7 | 2.4 |
| | JB776 | 78.3 | 0.5 | 0.8 | 0.3 | 0.2 | 0.0 | <0.01 | 7.5 | 12.3 | 100.0 | 0.1 | 2.2 | 1.4 | 0.6 | 1.7 |
| Type 2 | JB630 | 50.6 | 10.2 | 12.0 | 6.3 | 7.0 | 1.4 | 0.3 | 2.5 | 8.9 | 100.3 | 0.1 | 0.7 | | | |
| | JB777 | 44.2 | 6.4 | 13.1 | 5.0 | 3.8 | 0.4 | 0.1 | 2.3 | 24.2 | 99.8 | 0.2 | 2.6 | 6.0 | 2.4 | 0.1 |
| Type 3 | JB631-1 | 43.3 | 10.6 | 11.8 | 13.0 | 4.3 | 0.7 | 0.1 | 1.7 | 13.5 | 99.9 | 0.0 | 0.3 | | | |
| | JB631-2 | 42.4 | 12.3 | 11.2 | 10.1 | 3.0 | 0.5 | 0.1 | 1.7 | 17.7 | 99.8 | 0.1 | 0.4 | 1.1 | 0.4 | 0.0 |
| Type 4 | JB775 | 15.9 | 0.1 | 0.2 | 0.1 | 0.2 | 0.0 | <0.01 | 1.4 | 82.1 | 100.0 | 0.1 | 66.3 | 1.2 | 0.5 | 65.8 |

**Table 2b** **Minor elements in parts per million (ppm)**

| Sample Type | Sample ID | $P_2O_5$ ppm | MnO ppm | $Cr_2O_3$ ppm | Cu ppm | Ba ppm | Zn ppm | Ni ppm | Co ppm | Sr ppm | Zr ppm | Ce ppm | Y ppm | Nb ppm | Sc ppm |
|---|---|---|---|---|---|---|---|---|---|---|---|---|---|---|---|
| | JB629-1 | 300 | 100 | 290 | | 163 | | 5 | | 7 | 173 | | 5 | 21 | 1 |
| | JB629-2 | 600 | <100 | 380 | <5 | 125 | <5 | <20 | <20 | 7 | 169 | <30 | <3 | 19 | <1 |
| | JB632 | 800 | <100 | 1180 | <5 | 372 | 6 | <20 | <20 | 8 | 247 | <30 | <3 | 56 | <1 |
| | JB776 | 400 | <100 | 960 | <5 | 253 | <5 | <20 | <20 | 6 | 173 | <30 | <3 | 43 | 1 |
| Type 2 | JB630 | 2200 | 1100 | 770 | | 129 | | 146 | | 243 | 139 | | 17 | 11 | 25 |
| | JB777 | 2000 | 800 | 700 | 94 | 88 | 58 | 105 | 23 | 105 | 130 | <30 | 7 | 11 | 18 |
| Type 3 | JB631-1 | 3800 | 1800 | 890 | | 85 | | 647 | | 119 | 91 | | 14 | 6 | 37 |
| | JB631-2 | 3800 | 1600 | 870 | 248 | 59 | 131 | 376 | 72 | 75 | 103 | <30 | 10 | 8 | 42 |
| Type 4 | JB775 | 100 | <100 | 190 | <5 | 9 | <5 | <20 | <20 | 6 | 56 | <30 | <3 | 14 | <1 |

Data are given in wt.%; Fe2O3T is total Fe and includes both Fe2+ and Fe3+; LOI is Loss on ignition at 1000 °C and includes C and S.

This is the peer-reviewed, final accepted version for American Mineralogist, published by the Mineralogical Society of America.
The published version is subject to change. Cite as Authors (Year) Title. American Mineralogist, in press.
DOI: https://doi.org/10.2138/am-2023-9153. http://www.minsocam.org/

**Table 3** **Microprobe analyses of sample regions**

| Sample Averages | $SiO_2$ wt.% | $Al_2O_3$ wt.% | $FeO^T$ wt.% | MgO wt.% | CaO wt.% | $Na_2O$ wt.% | $K_2O$ wt.% | $TiO_2$ wt.% | $SO_3$ wt.% | $P_2O_5$ wt.% | MnO wt.% | Sum wt.% |
|---|---|---|---|---|---|---|---|---|---|---|---|---|
| **JB629 silica glass** | 79.9 | 0.5 | 0.2 | 0.0 | 0.0 | 0.0 | 0.0 | 2.8 | 1.5 | 0.2 | 0.0 | 85.1 |
| **JB629 silica rinds** | 70.2 | 0.6 | 0.5 | 0.1 | 0.1 | 0.1 | 0.0 | 1.8 | 0.6 | 0.0 | 0.0 | 73.9 |
| **JB629 bulk XRF** | 80.5 | 0.4 | 0.7 | 0.1 | 0.1 | 0.0 | 0.0 | 3.4 | 0.0 | 0.1 | 0.0 | 85.1 |
| **JB630 glass** | 49.6 | 13.0 | 11.2 | 8.3 | 10.5 | 2.2 | 0.4 | 2.4 | 0.1 | 0.3 | 0.2 | 98.2 |
| **JB630 rinds** | 57.5 | 19.6 | 9.8 | 2.0 | 0.8 | 0.1 | 0.1 | 2.2 | 0.2 | 0.2 | 0.1 | 92.5 |
| **JB631 glass** | 49.5 | 13.0 | 11.1 | 8.5 | 10.3 | 2.3 | 0.4 | 2.4 | 0.1 | 0.3 | 0.1 | 98.1 |
| **JB631 rind** | 46.0 | 11.0 | 20.2 | 3.8 | 0.1 | 0.0 | 0.0 | 4.2 | 0.4 | 0.1 | 0.1 | 86.0 |
| **JB631 Mg-smectite** | 50.2 | 17.3 | 4.5 | 14.8 | 0.1 | 0.0 | 0.0 | 0.0 | 1.0 | 0.7 | 0.7 | 89.3 |
| **JB631 bright spots** | 1.7 | 10.1 | 48.3 | 0.1 | 0.0 | 0.0 | 0.0 | 0.1 | 9.2 | 4.1 | 0.0 | 73.7 |
| **JB631 ave all types** | 36.8 | 12.8 | 21.0 | 6.8 | 2.7 | 0.6 | 0.1 | 1.7 | 2.7 | 1.3 | 0.2 | 86.8 |
| **JB631 weighted ave** | 43.3 | 14.0 | 14.4 | 9.2 | 3.9 | 0.9 | 0.1 | 1.5 | 1.6 | 0.9 | 0.3 | 90.2 |
| **JB631 bulk XRF** | 42.4 | 12.3 | 10.1 | 10.1 | 3.0 | 0.5 | 0.1 | 1.7 | 0.0 | 0.4 | 0.2 | 80.8 |
| **Keanakako'i Glass** | 50.1 | 12.8 | 11.2 | 9.2 | 10.3 | 2.2 | 0.4 | 2.2 | | 0.3 | 0.2 | 98.9 |

Data are given in wt.%, FeOT is total Fe and includes both Fe2+ and Fe3+; Sum includes only elements listed
Keanakako'i Glass data are an average of 23 measurements (Schiffman et al. (2000)

This is the peer-reviewed, final accepted version for American Mineralogist, published by the Mineralogical Society of America.
The published version is subject to change. Cite as Authors (Year) Title. American Mineralogist, in press.
DOI: https://doi.org/10.2138/am-2023-9153. http://www.minsocam.org/

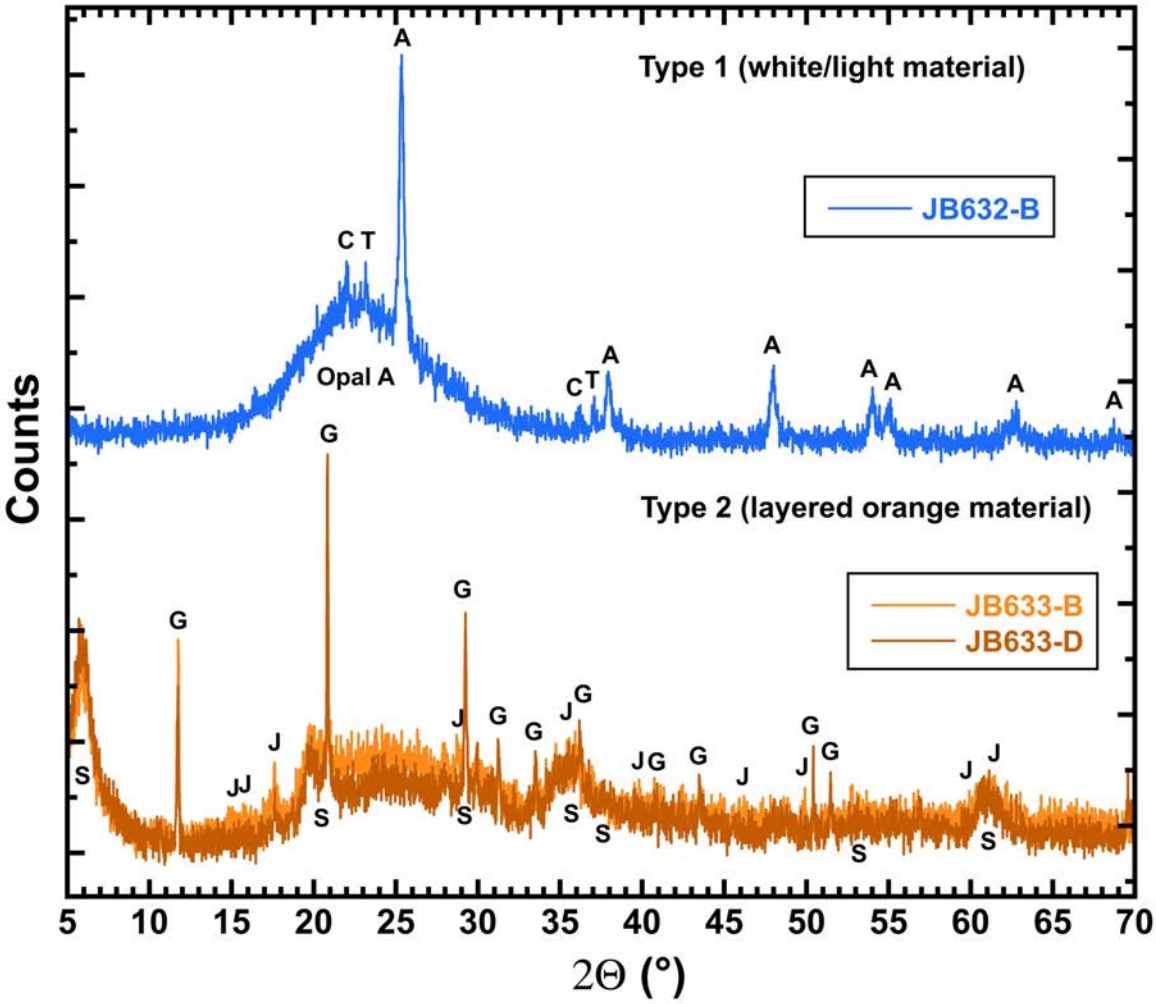


**Figure 4 XRD of <125 µm portions of selected samples from the light and orange materials.** Sample JB632-B (Type 1, white/light material) contains the broad peak near 20-25 °2Θ characteristic of opal A, as well as strong peaks due to anatase (A), and weak peaks due to cristobalite (C) and tridymite (T). Samples JB633-B and JB633-D (Type 2, layered orange material) are separate aliquots of JB633, each sieved to <125 µm. Both contain multiple, broad peaks due to Mg-smectite and Fe-smectite (S), several strong peaks due to gypsum, and several weaker peaks due to jarosite (J).

This is the peer-reviewed, final accepted version for American Mineralogist, published by the Mineralogical Society of America.
The published version is subject to change. Cite as Authors (Year) Title. American Mineralogist, in press.
DOI: https://doi.org/10.2138/am-2023-9153. http://www.minsocam.org/

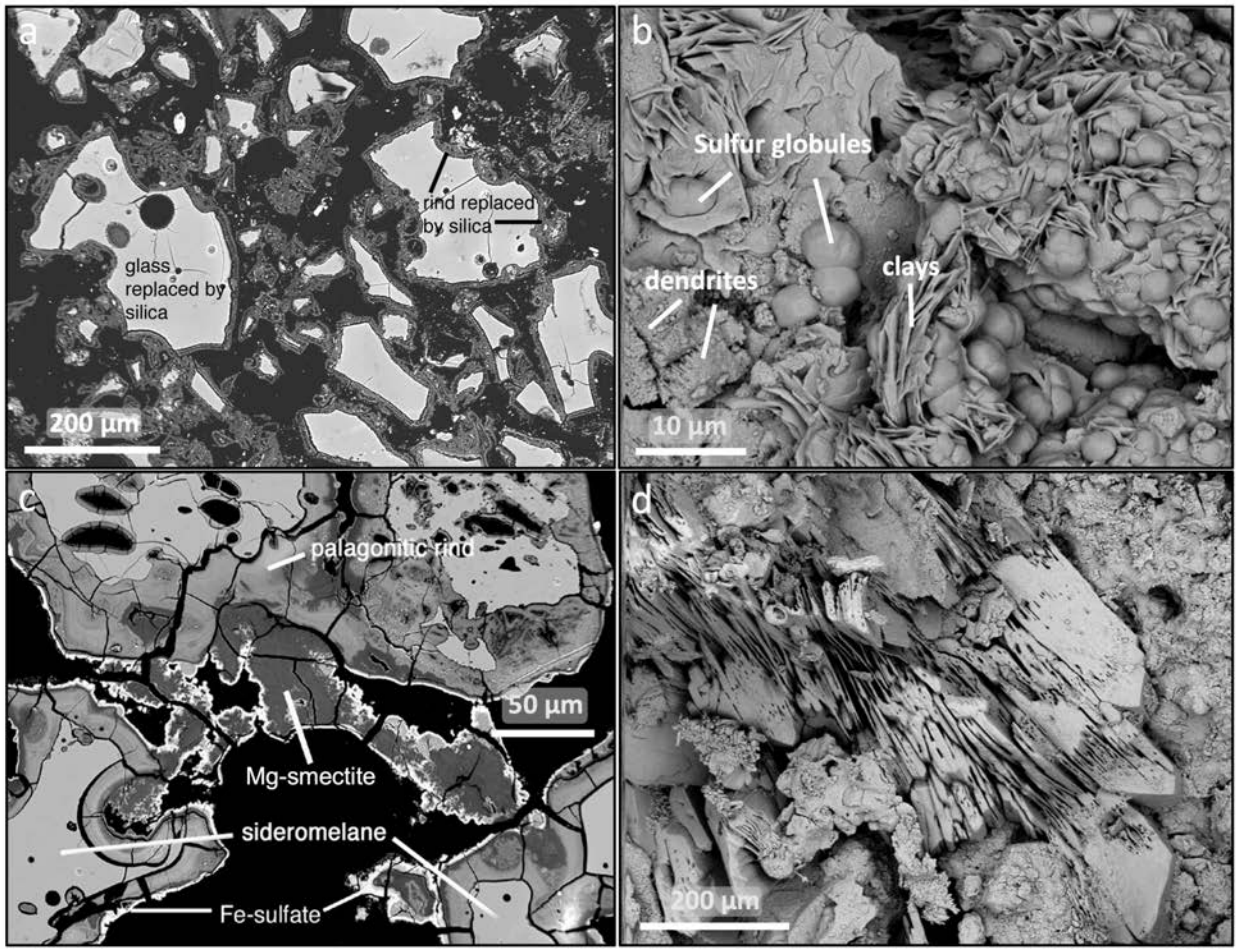


**Figure 5 SEM images showing altered phases in selected light and orange materials.** a) View of glassy grains and rinds replaced by silica in EMPA map of sample JB629 (Type 1, white/beige material). b) Sulfur globules, platy aluminosilicate, and relict primary dendrites in a yellow portion of sample JB629 under high magnification in a BSE image. c) EMPA view of altered phases in orange layers of sample JB631 (Type 3, gray/orange material) including Mg-smectite (saponite or hectorite) and Fe-sulfate (jarosite). d) Gypsum in lighter layers in BSE image of sample JB630 (Type 2, orange material).

## VNIR and TIR spectra of bulk samples

VNIR reflectance spectra of rock samples measured under ambient conditions demonstrate compositional variations among the samples investigated, although the water bands are rather strong due to adsorbed $H_2O$ molecules on the surfaces (Figure 6). The lighter colored samples contain broad bands centered near 1.41-1.47, 1.91-1.95, and 2.21-2.27 µm due to abundant opal and some montmorillonite, jarosite, and gypsum, but no alunite was observed (e.g., Bishop 2019). The spectral features near 1.4 µm include the Si/Al-OH stretching overtone at 1.41 µm, the bound $H_2O$ stretching overtone at 1.41 µm, and the lower energy adsorbed $H_2O$ stretching overtone near

1.44-1.45 µm (Bishop et al. 1994). A shoulder on the short-wavelength side of this band near 1.37 µm is attributed to the Si-OH stretching overtone for dehydrated opal (Anderson and Wickersheim 1964). The band at 1.91 µm is due to a combination of $H_2O$ stretching and bending vibrations for tightly bound water molecules in opal and smectites, while the shoulder near 1.94-1.95 µm is due to the $H_2O$ combination band for adsorbed or more loosely bound water molecules (Bishop et al. 1994). Additional $H_2O$ overtones occur as weaker bands near 0.96 and 1.15 µm. The band near 2.21-2.27 µm is due to a combination of structural OH stretching and bending vibrations and occurs near 2.21 µm for Si/ Al-OH and at longer wavelengths for Fe/Mg-OH (e.g., Bishop et al. 2008a). The VNIR spectra are also consistent with the presence of Fe-bearing opal (Baker et al. 2014) that exhibits a broader band near 2.2 µm extending out towards 2.26 µm. Both jarosite (Bishop and Murad 2005) and gypsum (Bishop et al. 2014) also have features at 2.22 and 2.26 µm that contribute towards the broadening of this band. Jarosite spectra also include a sharp band at 1.47 µm that is likely contributing to the doublet-like shape at 1.41 and 1.47 µm for coarse material of samples JB629 and JB776 (Figure 6b). The VNIR spectra of the light-toned solfatara rocks resemble the spectra of solfatara rocks measured in the Ka'u Desert as well as aerial spectra of solfatara regions collected by AVIRIS (Seelos et al. 2010).

The orange and darker colored samples are more variable in the VNIR region and include bands near 0.44 and 0.9-1 µm due to Fe, as well as the $H_2O$ and OH bands described for the lighter colored samples (Figure 6a,c,d). The reflectance minimum near 0.91 µm and maximum near 0.73-0.74 µm is consistent with jarosite as well as akaganéite and schwertmannite (Bishop and Murad 1996), but only jarosite was observed by XRD. Ferrihydrite is also consistent with a band near 0.91 µm and is X-ray amorphous so it could also be present. The weak dip in reflectance near 0.63-0.64 µm and shoulder near 0.88 µm likely indicates that some nanophase hematite is present (e.g., Morris et al. 1985; 1989; Bishop and Murad 1996) that is too fine-grained or poorly crystalline to be observed with XRD. Fe in nontronite also produces bands near 0.64-0.65 and 0.95 µm (Bishop et al. 2008b) that could be contributing to these features in spectra of the orange samples. A triplet near 1.44, 1.49-, and 1.53, and bands near 1.75, and 1.94 µm are characteristic of gypsum (Bishop et al. 2014) and these features are much more apparent in some of the orange-colored samples than the friable, light-toned ones. Weak bands due to jarosite are observed at 1.47 and 2.26 µm, but the jarosite band near 1.86 µm is not observed, indicating that jarosite abundance is less than 50 wt.% (Perrin et al. 2018; Usabal and Bishop 2018). Spectra of orange soils from the sulfate hill at the

This is the peer-reviewed, final accepted version for American Mineralogist, published by the Mineralogical Society of America.
The published version is subject to change. Cite as Authors (Year) Title. American Mineralogist, in press.
DOI: https://doi.org/10.2138/am-2023-9153. http://www.minsocam.org/

388 Painted Desert include jarosite (52 wt.%) and gypsum (26 wt.%) that exhibit jarosite bands at 0.44,
389 0.91, 1.47, 1.86, and 2.26 µm (Perrin et al. 2018) and lab spectra of jarosite/gypsum mixtures
390 (Perrin et al. 2018) and jarosite/nontronite mixtures (Usabal and Bishop 2018) with 50 wt.%
391 jarosite include a shoulder at 1.86 µm.
392

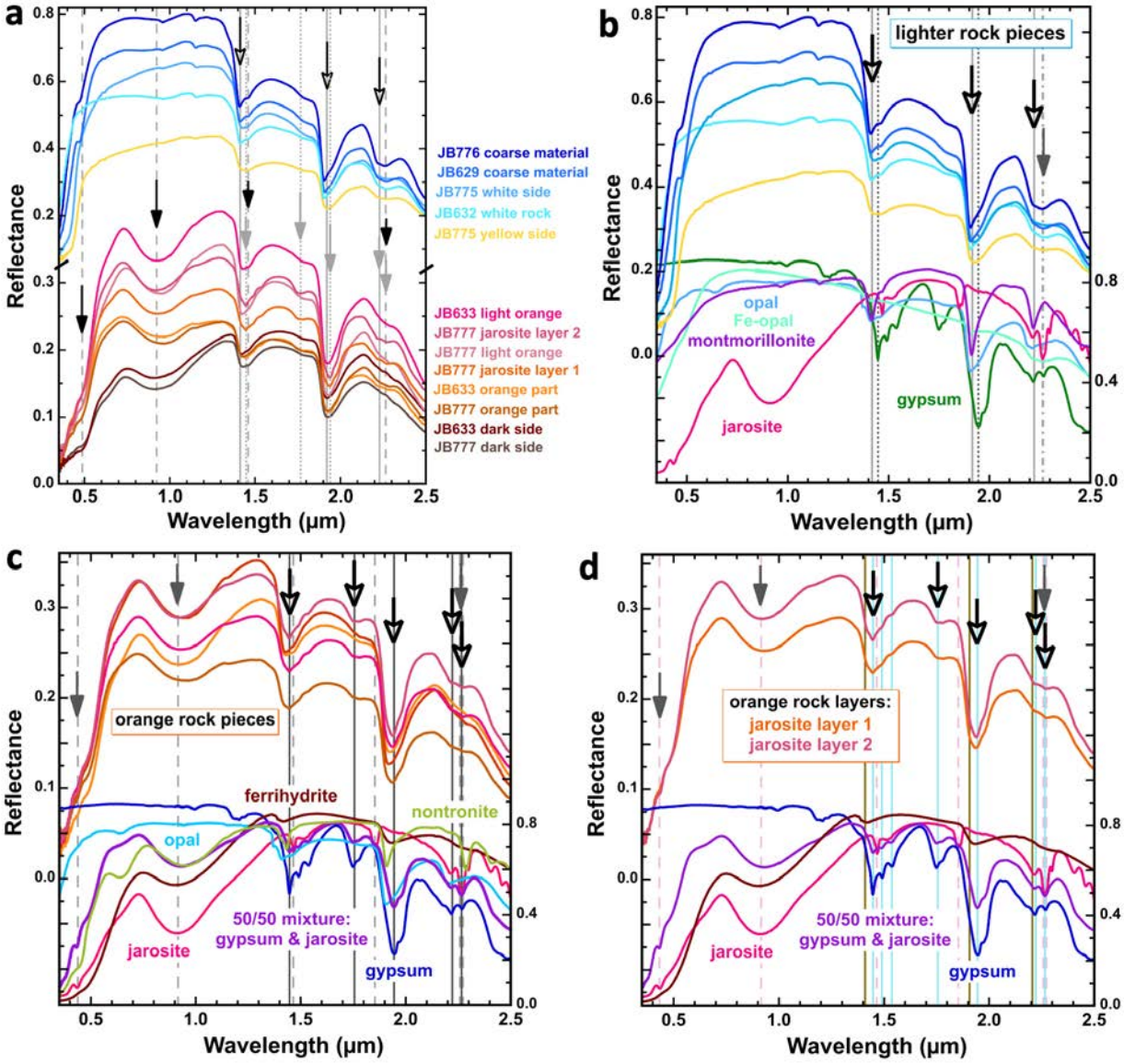


393
394
395 **Figure 6. VNIR reflectance spectra (0.35-2.5 µm) of rock samples collected with ASD**
396 **spectrometer.** a) Spectra of light and dark materials where white/beige rocks have brighter
397 reflectance than orange/dark rocks. Open arrows mark features due to opal near 1.41,1.91, 2.21
398 µm, black arrows mark features due to jarosite near 0.44, 0.91, 1.47, and 2.26 µm, and gray arrows
399 mark features due to gypsum near 1.45, 1.75, 1.94, 2.22, and 2.26 µm. b) Spectra of lighter rock
400 pieces compared with spectra of minerals: opal, Fe-opal, montmorillonite, jarosite, and gypsum.

Open arrows mark features due to opal and solid arrow marks feature near 2.26 μm that could be due to Fe substitution in the opal or to jarosite. c) Spectra of orange rock pieces compared with spectra of minerals: opal, ferrihydrite, nontronite, jarosite, gypsum, and a jarosite/gypsum mixture. Open arrows mark features due to gypsum and filled arrows mark features due to jarosite. c) Spectra of orange rock layers containing stronger jarosite spectral signatures compared with spectra of jarosite, gypsum, a jarosite/gypsum mixture, and ferrihydrite. Open arrows and light blue lines mark features due to gypsum, while filled arrows and light pink dashed lines mark features due to jarosite.

TIR emissivity spectra measured in the mid-IR region of the orange side of sample JB633 include features due to gypsum and jarosite (Figure 7). The emissivity spectrum of jarosite includes features near 1110, 1020, 630, 525, 475, and 250 $cm^{-1}$ (or ~9, 10, 16, 19.6, 21, and 40 μm), while that of gypsum has features at ~1154, 673, 604, and 470 $cm^{-1}$ (or ~8.7, 15, 17, and 21 μm). These are similar to jarosite and gypsum bands observed in previous studies (Lane and Christensen 1998; Bishop and Murad 2005; Bishop et al. 2014). Sulfates exhibit strong $SO_4$ stretching and bending vibrations in this region (Lane and Bishop 2019) that often dominate the spectral features of phyllosilicates and opal. These strong bands in the emissivity spectrum are why the emissivity spectrum of the orange layered rock is primarily characterized by gypsum and jarosite, rather than poorly crystalline phases.

This is the peer-reviewed, final accepted version for American Mineralogist, published by the Mineralogical Society of America.
The published version is subject to change. Cite as Authors (Year) Title. American Mineralogist, in press.
DOI: https://doi.org/10.2138/am-2023-9153. http://www.minsocam.org/

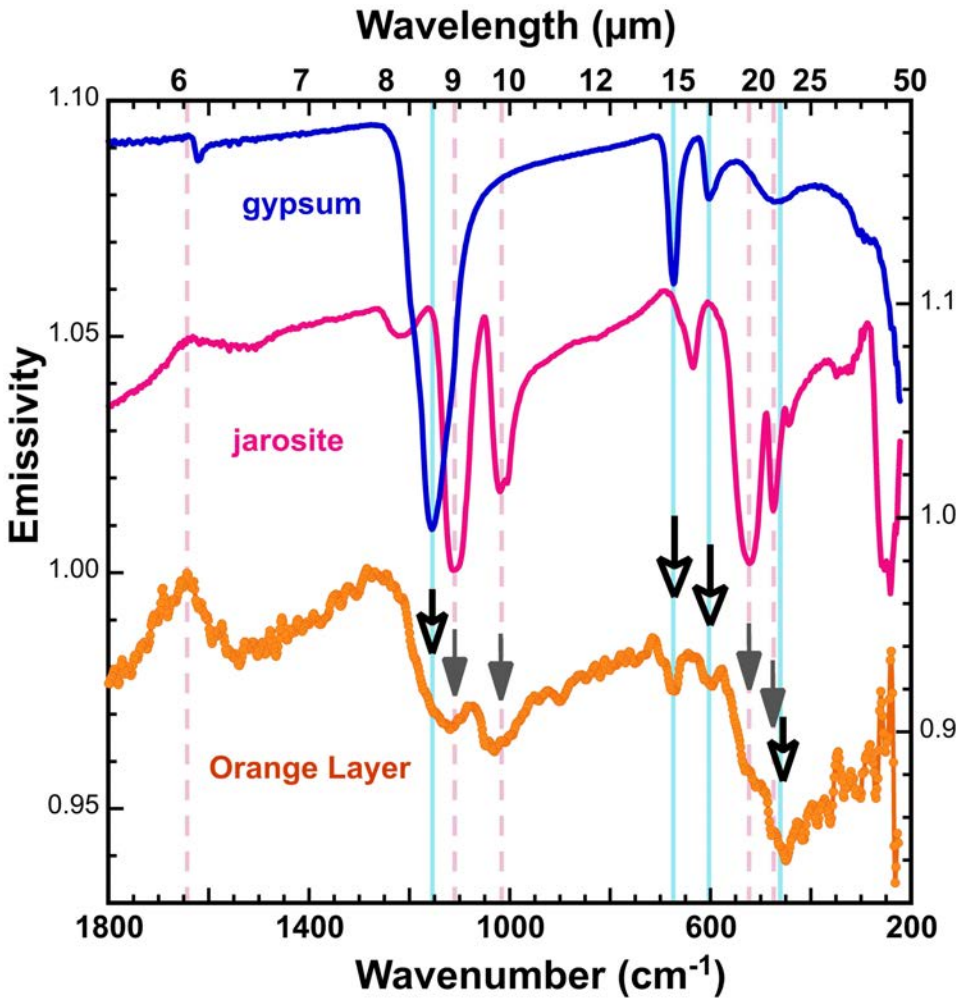


**Figure 7. Emissivity spectra of orange rock (JB633) and sulfate minerals.** Blue lines indicate gypsum features near 1154, 673, 604, and 470 $cm^{-1}$ and dashed pink lines mark jarosite features near 1645, 1110, 1020, 525, and 475 $cm^{-1}$.

## VNIR and mid-IR reflectance spectra of particulate samples

Reflectance spectra of fine-grained portions of the samples measured under controlled, dry conditions exhibit weaker water bands that are more characteristic of specific minerals in many cases (Figure 8) compared to spectra of rocks measured under ambient conditions (Figure 6). VNIR and mid-IR reflectance spectra of the white/light samples JB629-B and JB632-B are compared with spectra of opal, montmorillonite, and bytownite (Figures 8a,b). Although opal is the most abundant component in these samples due to hydration of the silica replacing the glass and rinds, some features characteristic of montmorillonite and feldspar are also present. These spectra illustrate the NIR features due to opal and montmorillonite near 1.41,1.91, and 3 μm

This is the peer-reviewed, final accepted version for American Mineralogist, published by the Mineralogical Society of America.
The published version is subject to change. Cite as Authors (Year) Title. American Mineralogist, in press.
DOI: https://doi.org/10.2138/am-2023-9153. http://www.minsocam.org/

(Bishop 2019), as well as mid-IR features due to opal near 1875, 1260, 1105 and 475 $cm^{-1}$ (Bishop and Rampe 2016), the montmorillonite water band near 1630 $cm^{-1}$, and the feldspar Si-O stretching band as a reflectance peak near 1000 $cm^{-1}$.

Spectra of fine-particulate portions of the darker orange and tan samples are compared to spectra of the minerals nontronite, saponite, opal, gypsum, and jarosite in Figures 8c and d. The spectra of these samples differ from the spectra of the light-toned samples in that phyllosilicates and sulfates contribute more to the spectral character than opal. A band near 0.91-0.95 µm is due to Fe-bearing minerals in these samples and varies from sample to sample with variations in nontronite, jarosite, and iron oxide minerals that are likely present as short-range ordered species that are not sufficiently crystalline to be detected by XRD. Bands near 1.41 and 1.91 µm are characteristic of water overtones and combinations in opal and smectites, while the band near 2.21 µm is due to an OH combination band in spectra of opal or montmorillonite, the band near 2.29 µm is due to nontronite, and the band near 2.31 µm is due to saponite or hectorite (Mg-rich smectites). Gypsum and jarosite also have features near 2.22 and 2.27 µm that overlap with these smectite bands. Gypsum also has bands near 4.5 and 4.7 µm observed for some of these samples. The mid-IR region for these samples is most consistent with spectra of Mg-smectite with some features due to gypsum. Expanded NIR views of samples JB633-B and JB643-A include several features due to nontronite, opal, and gypsum (Figure 8e). The water combination band occurs near 1.95 µm in these samples, similar to that of gypsum, with a shoulder near 1.91 µm due to nontronite or opal. NIR spectra of samples JB631-B and JB631-D are consistent with Mg-smectite and opal, while NIR spectra of JB630-B includes weak features due to jarosite at 1.47, 2.22 and 2.27 µm, in addition to bands characteristic of opal near 1.37, 1.41, 1.91, and 2.21 µm (Figure 8f).

This is the peer-reviewed, final accepted version for American Mineralogist, published by the Mineralogical Society of America.
The published version is subject to change. Cite as Authors (Year) Title. American Mineralogist, in press.
DOI: https://doi.org/10.2138/am-2023-9153. http://www.minsocam.org/

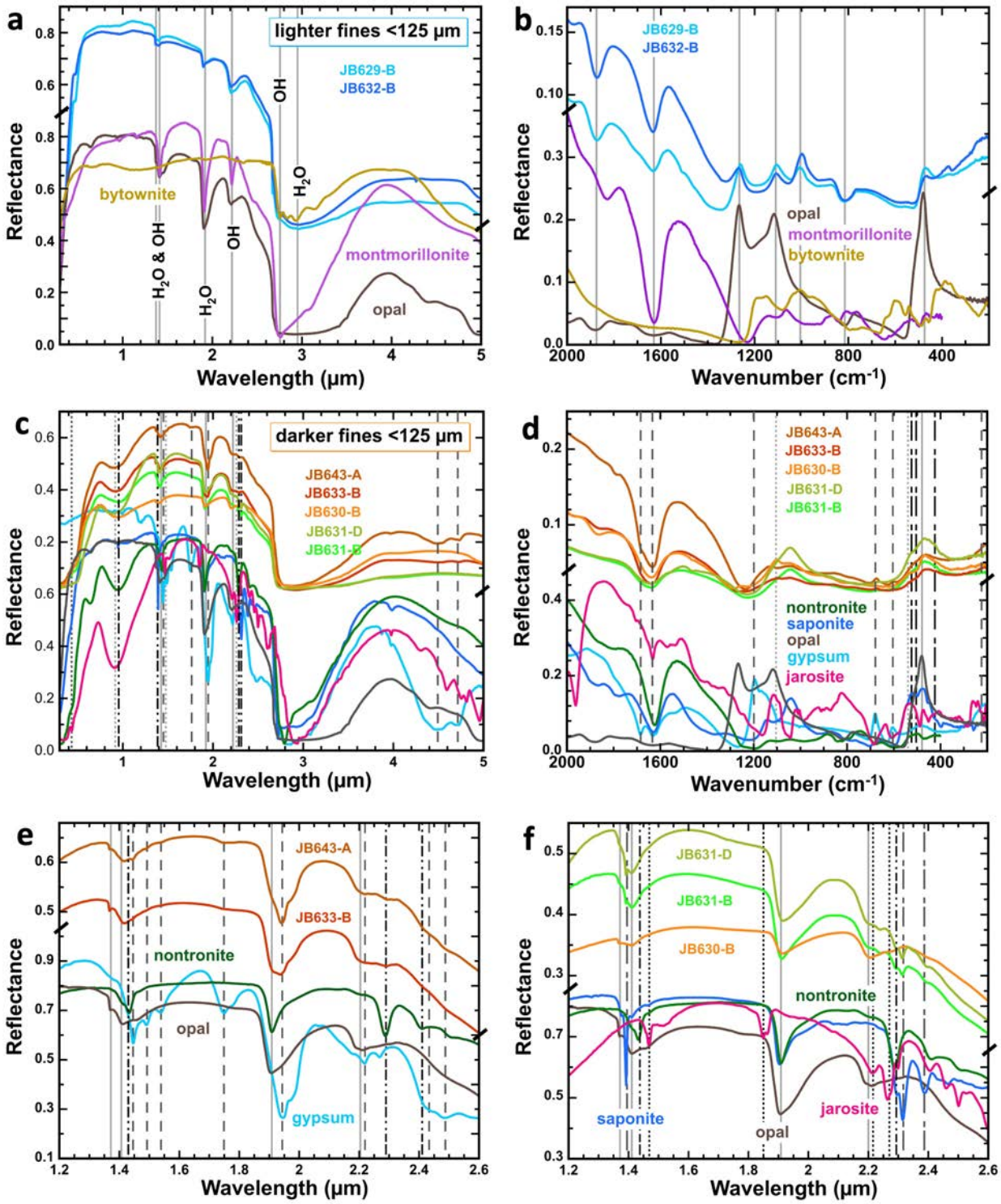


**Figure 8. VNIR and mid-IR reflectance spectra of fine-grained solfataric samples.** a-b) Spectra of lighter-colored fines compared to spectra of opal, bytownite, and montmorillonite. Solid gray lines mark features due to $H_2O$ in opal and montmorillonite near 1.41,1.91, and 3 µm, plus near 1630 $cm^{-1}$. Features due to OH in opal and montmorillonite are observed near 1.41, 2.2, and 2.7 µm. Additional opal bands near 1875, 1260, 1105 and 475 $cm^{-1}$ and a feldspar band near 1000 $cm^{-1}$ are also found in spectra of the light-colored samples. c-d) Spectra of darker-colored fines

compared to spectra of nontronite, saponite, opal, gypsum, and jarosite. Opal is less abundant in these samples and contributes to features near 1.4, 1.9, and 2.2 µm, marked by solid gray lines. Light gray dotted lines mark features due to jarosite at 0.44, 0.91, 1.47, and 2.26 µm, as well as near 1105 and 540 $cm^{-1}$. Gray dashed lines mark features due to gypsum at 1.45, 1.75, 1.94, 2.22, 2.26, 4.5, and 4.7 µm, as well as near 1680, 1635, 1200, 680, 600, and 220 $cm^{-1}$. Black broken lines mark features due to nontronite at 0.95, 1.43, and 2.29 µm and near 500 and 420 $cm^{-1}$, and due to saponite at 1.39, 2.31 µm and near 525 $cm^{-1}$. e) Expanded view of JB633-B and JB643-A spectra that include features due to gypsum, opal, and nontronite. f) Expanded view of JB630-B, JB631-B, and JB631-D spectra that include features due to opal, nontronite, saponite, and jarosite.

## Mössbauer spectroscopy

Mössbauer spectra of samples of the white/light (JB632) and orange (JB633) materials are shown in Figure 9 together with spectra of selected minerals. The white/light and orange/tan materials are subtly different, but both have contributions from ferrihydrite, which has parameters of isomer shift (IS) = 0.35 mm/s and quadrupole splitting (QS) = 0.71 mm/s for single doublet fits (Murad and Schwertmann 1980). The spectrum of JB632 has a doublet with IS of 0.37 mm/s and QS of 0.55 mm/s, consistent with a poorly crystalline ferric oxide-bearing phase similar to ferrihydrite. The VNIR spectra of sample JB632 are consistent with the presence of Fe-bearing opal and that could also explain the ferrihydrite-like component of the Mössbauer spectrum. Another contribution to the Mössbauer spectrum of sample JB632 is from saponite, which also observed in the VNIR spectra and microprobe analyses.

The spectrum of JB633 has a well-formed doublet with isomer shift of 0.39 mm/s and quadrupole splitting of IS of 0.65 mm/s that is more similar to ferrihydrite than nontronite or jarosite, but may again include a contribution from saponite or alternatively a ferrous sulfate (Dyar et al. 2013).

This is the peer-reviewed, final accepted version for American Mineralogist, published by the Mineralogical Society of America.
The published version is subject to change. Cite as Authors (Year) Title. American Mineralogist, in press.
DOI: https://doi.org/10.2138/am-2023-9153. http://www.minsocam.org/

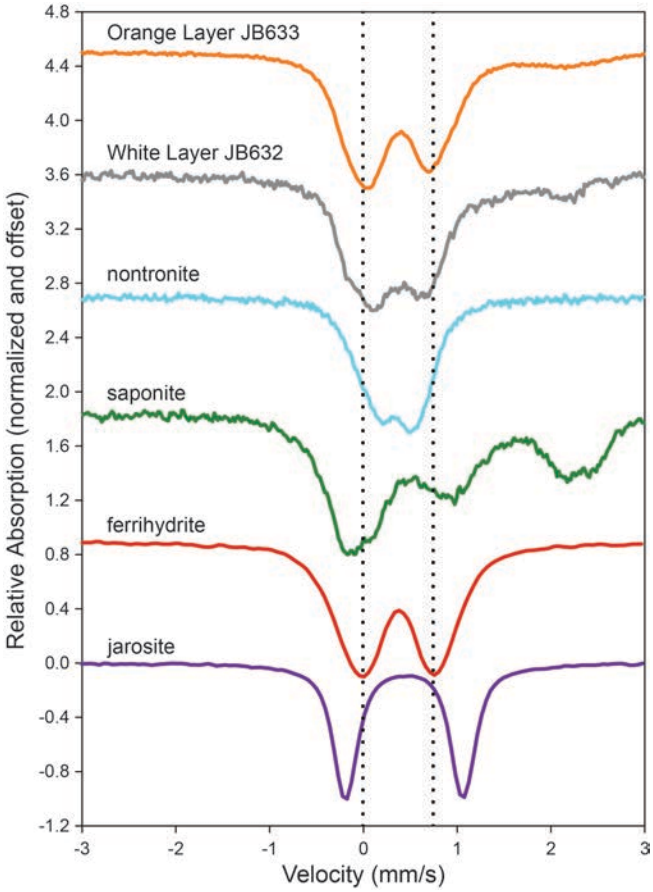


**Figure 9. Mössbauer spectra of solfatara samples compared with minerals.** Spectra of the white/light (JB632) and orange (JB633) samples are composed of doublets consistent with primarily $Fe^{3+}$ and some $Fe^{2+}$ in minerals. Mineral spectra are presented for saponite (103), nontronite (JB175), ferrihydrite (JB499), and jarosite (132066). The vertical lines mark the doublet observed for ferrihydrite and related poorly crystalline ferric oxide species that are similar to the doublets observed in spectra of both the white/light and orange samples.

## Discussion

### Comparison with other terrestrial analog sites

Investigation of hydrothermally altered volcanic material at other field sites in Hawaii, Iceland, LaSolfatara, Yellowstone, Southwestern Australia, and the Atacama has identified similar mineral assemblages in some cases, although the presence of jarosite, gypsum, and smectite is uncommon. Silica was observed as the primary alteration product through hydrothermal alteration of basaltic lavas from the Kilauea 1974 flow (Yant et al. 2017) near our field site. Yant et al. (2017) also observed small amounts of jarosite, gypsum, phyllosilicates, and iron oxide phases in some samples from their study. Assemblages of jarosite, silica, and hydrated ferric oxides were identified in crusted material in the Kilauea region where plumes bearing sulfuric acid likely

515 altered the volcanic ash in an acid-fog type mechanism (Schiffman et al. 2006). Hydrothermal
516 alteration at Haleakala volcano on Maui produced jarosite and alunite near some of the cinder
517 cones inside the caldera, along with poorly crystalline Al-Si phases, silica, smectites, and iron
518 oxides/hydroxides (Bishop et al. 2007). Assemblages containing jarosite, alunite, and silica were
519 observed near fumaroles at the Italian Solfatara, but this site was too acidic for formation of
520 smectite or gypsum (Flahaut et al. 2019). Another acid hydrothermal site at Yellowstone National
521 Park produced jarosite, other low-pH sulfates, and kaolinite, but not gypsum or smectite (Hinman
522 et al. 2021). The abundance of jarosite at the Italian Solfatara and Yellowstone sites could be due
523 to the elevated temperatures and low acidity at these sites. Gypsum has been found in a variety of
524 environments on Earth, but is more commonly observed in evaporite or high saline environments
525 (e.g., Benison and Bowen 2006; Bowen et al. 2013; Flahaut et al. 2017; Bishop et al. 2021b; Burton
526 et al. 2023; Warren-Rhodes et al. 2023). Gypsum can also form in hydrothermal environments and
527 is then often accompanied by carbonates (Burisch et al. 2018). Gypsum, jarosite, and smectite have
528 been observed together at the Sulfate Hill in the Painted Desert region of the Petrified Forest
529 (Perrin et al. 2018), although the genesis of this site is not yet well understood. Gypsum and jarosite
530 have been detected together in saline lakes, where halite, silica or kaolin minerals are frequently
531 observed as well, but smectite is less common in these areas (e.g., Benison and Bowen 2006;
532 Bowen et al. 2013).

533 Solfataric alteration at other fumarole sites has produced similar alteration trends to our
534 observations at the Kilauea South Sulfur Banks site. Pyroclastic basalts altered by the Cerro Negro
535 fumaroles in Nicaragua resulted in amorphous silica, gypsum, alunite/jarosite, and iron
536 oxides/oxyhydroxides (McCollom et al. 2013). The Námafjall geothermal area in Iceland harbors
537 a range of alteration environments and products including amorphous silica, anatase, elemental S,
538 smectite, kaolinite, goethite, sulfides, and multiple $Fe^{2+}$ and $Fe^{3+}$ sulfates, formed under acidic
539 conditions near hot springs (Carson et al. 2023b). Pyrite and other sulfides were only found at
540 depth in that study and not near the surface. A second study at the Námafjall geothermal area
541 investigated changes in alteration with distance from the Hverir fumarole (Carson et al. 2023a)
542 and found native S closest to the vent in soils enriched in silica and anatase, similar to the
543 white/light-colored silica-bearing apron in our study that included yellow native S near the vent
544 (Figures 2,3,10). Cristobalite was abundant in the light-toned soils close to the Hverir vent site,
545 whereas opal-A was most abundant and only trace cristobalite was observed in our study, likely

546 indicating lower temperatures at the Kilauea South Sulfur Bank site. Further from the Hverir
547 fumarole vent jarosite and alunite were observed together with kaolinite and hematite, and still
548 further out from the vent smectite was observed (Carson et al. 2023a). Temperatures ranged from
549 ~14 to 97 °C where samples were collected near the Hverir fumarole. Temperature was not
550 recorded during sampling at the Kilauea South Sulfur Bank site, but elevated temperatures were
551 not noticed while working at the Kilauea South Sulfur Bank site. During our visits to the South
552 Sulfur Bank site in 2003-2006, small vents with periodic wisps of gases and/or steam emanating
553 from one or more vents was observed, rather than a continuous outpouring of steam observed at
554 other more active fumarole sites. Historic activity at the South Sulfur Bank site could have been
555 different. The moderate temperatures of the vents observed during our field work are consistent
556 with formation of the assemblages of opal-A, gypsum, smectite, poorly crystalline ferric oxide
557 phases, and minor jarosite, based on comparison with these other hydrothermal alteration studies.
558 It is possible that the jarosite, trace cristobalite, and trace tridymite at the South Sulfur Bank site
559 formed during past episodes of greater steam activity at higher temperatures. If this were the case,
560 the jarosite, cristobalite, and tridymite would have been little altered by the mild steam activity
561 observed at the time of sampling. Hydrothermal alteration at other sites at elevated temperatures
562 produced higher quantities of jarosite and/or alunite together with cristobalite, kaolinite, and
563 hematite, instead of smectite and poorly crystalline ferric oxide phases.

564 Alteration at the South Sulfur Bank site includes oxidation and leaching of the basaltic lava
565 covering the pyroclastic deposit, alteration of the orange/tan banded outcrop, and alteration of the
566 white/light soil (Figure 10). The four different alteration types observed are highlighted in a
567 schematic diagram of the site in Figure 11. The friable white/light material is closest to the vents
568 at the floor of the South Sulfur Bank and the glass and rinds are both replaced by ~80 wt.% silica.
569 Hydrated silica, anatase, and native S are the primary components of this friable unit, similar to
570 the highly altered material observed closest to the Hverir fumarole in Iceland (Carson et al. 2023a).
571 The opal-A measured in our study likely results from lower temperature hydrothermal alteration
572 compared to the Hverir fumarole where temperatures close to 100 °C were observed and
573 cristobalite formed rather than opal-A, indicating much higher temperatures at that site.

This is the peer-reviewed, final accepted version for American Mineralogist, published by the Mineralogical Society of America.
The published version is subject to change. Cite as Authors (Year) Title. American Mineralogist, in press.
DOI: https://doi.org/10.2138/am-2023-9153. http://www.minsocam.org/

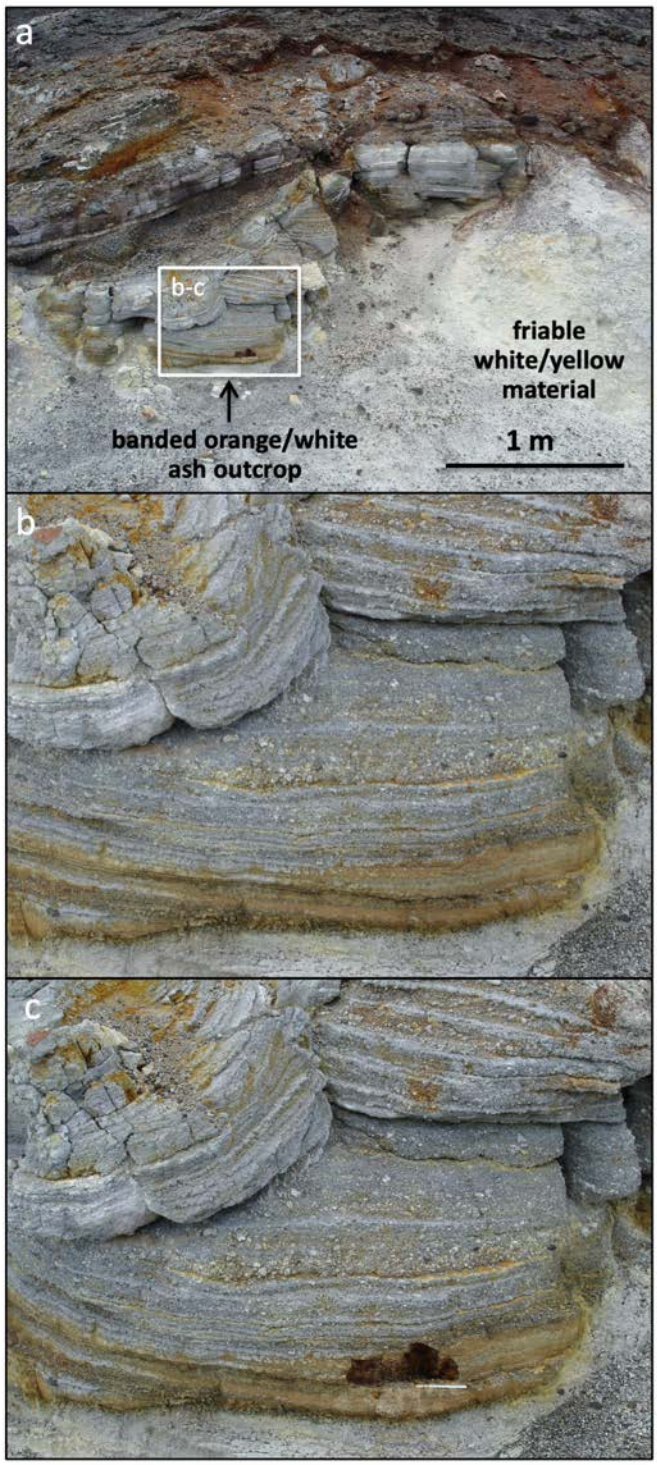


**Figure 10. Solfatarically altered Keanakakoi ash deposit at Kilauea South Sulfur Bank.** a) View in 2006 of the bedded orange/beige pyroclastic units and friable white/yellow material underneath the altered basaltic flow, b) bedded orange/beige layers (note change since 2004 in Figure 3 such that layered material has been eroded and previous sample collection site is not observed), c) same view as b after collecting sample; pH indicator stick in fresh hole below the surface of the banded orange material shows pH ~3-4.

This is the peer-reviewed, final accepted version for American Mineralogist, published by the Mineralogical Society of America.
The published version is subject to change. Cite as Authors (Year) Title. American Mineralogist, in press.
DOI: https://doi.org/10.2138/am-2023-9153. http://www.minsocam.org/

581

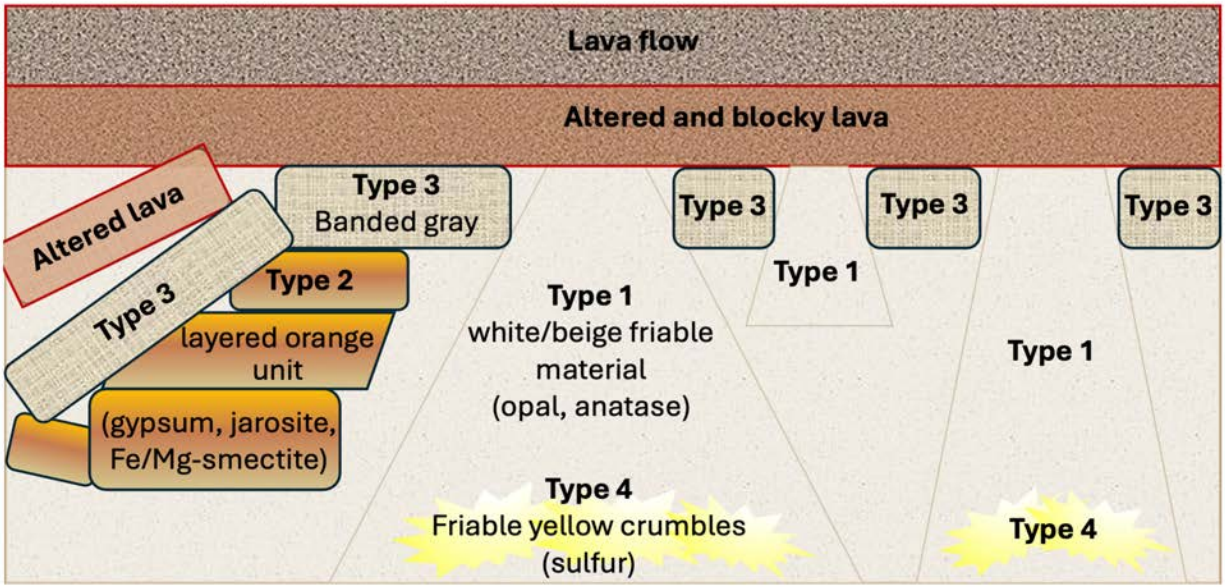


582

583 **Figure 11. Schematic diagram of study site.** Approximate relationships of the four types of
584 alteration documented in this study. Type 1 is the white/beige friable material descending from the
585 altered, blocky lava and primarily composed of opal and anatase. Type 2 is the layered orange and
586 grey unit that contains gypsum, jarosite, nontronite, and Mg-smectite. Type 3 is the banded gray
587 unit that is positioned above the Type 2 unit and could be similar but less altered. Type 4 contains
588 the yellowish crumbles and rocks that include native sulfur (at the base of the Type 1 unit).

589

590 The orange/tan bedded units are further from the vents than the white/light/yellow friable
591 material and are much more consolidated. This banded region contains a combination of alteration
592 minerals in addition to some hydrated silica. Smectites include saponite, hectorite, and nontronite,
593 and the type of smectite present is likely governed by the cations that were available – nontronite
594 where Fe was readily available, hectorite where Mg and Li were available, and saponite where Mg
595 and Al were available. Feldspar and gypsum are observed with Mg-rich smectite in the tan/lighter
596 layers, whereas jarosite and poorly crystalline iron oxide phases are found with nontronite in the
597 orange layers. However, gypsum and Mg-smectites are also observed in some of the orange
598 material. Horizons of orange-colored beds are visible in several places, but patches of orange
599 material are also evident (Figure 10). This spatial relationship would suggest that there could have
600 been variations in the chemistry of the pyroclastic material as it was deposited, with elevated Fe
601 in some areas. Another possibility is that periodic episodes of greater leaching and alteration of
602 the basalt above this unit occurred and that altered material rich in ferric iron percolated down

This is the peer-reviewed, final accepted version for American Mineralogist, published by the Mineralogical Society of America.
The published version is subject to change. Cite as Authors (Year) Title. American Mineralogist, in press.
DOI: https://doi.org/10.2138/am-2023-9153. http://www.minsocam.org/

603 from the altered basalt and was collected in layers and patches at the banded pyroclastic unit below.
604 Possibly, boundaries at the beds in this unit could have helped retain the $Fe^{3+}$ to form a layer of
605 increased concentration of $Fe^{3+}$ to react with sulfates during alteration. The orange layers are not
606 just a thin surface coating, but extend at least 2 cm deep into the banded unit at the sampling
607 location (Figure 10c).

608

609

610 **Implications for Mars**

611 Characterization of analog sites with multiple mineralogy, chemistry, and spectroscopy
612 techniques provides data for interpretation of orbital and rover data at Mars. This study of high-
613 silica and smectite-sulfate outcrops near low-temperature vents at the South Sulfur Bank at Kilauea
614 provides an opportunity to investigate the minerals formed under moderate hydrothermal
615 conditions. These two types of hydrothermal outcrops are observed on Mars in ancient outcrops
616 and could have formed on Mars in the past under environmental conditions similar to the moderate
617 solfataric alteration that occurred at the Kilauea South Sulfur Bank region. The presence of high-
618 silica outcrops and smectite- gypsum- jarosite mixtures are still observed today in some regions of
619 Mars after billions of years. This indicates that limited liquid water has altered the surface since
620 the emplacement of these samples.

621 Martian outcrops with extremely high silica, similar to the friable, white material observed near
622 vents in the South Sulfur Banks region of Kilauea and near the Hverir fumaroles in Iceland are
623 found at the Home Plate hydrothermal system in Gusev crater (e.g., Rice et al. 2010; Ruff et al.
624 2011), at the Nili Patera caldera associated with Syrtis Major (Skok et al. 2010; Fawdon et al.
625 2015), and within the Murray and Stimson formations at Gale crater (Rapin et al. 2018). Siliceous
626 hot spring deposits are widespread on Earth (e.g., Campbell et al. 2015; Jones 2021) and have long
627 been considered potential ecosystems for life on Mars (e.g., Walter and Des Marais 1993; Farmer
628 1996; Schulze-Makuch et al. 2007; Cady et al. 2018). Opaline silica formed near low temperature
629 vents similar to the Kilauea South Sulfur Banks region could also have provided a niche for
630 potential microbes on Mars. An advantage in searching for life in ancient silica-rich outcrops on
631 Mars is the high preservation potential in such environments (Walter and Des Marais 1993; Farmer
632 and Des Marais 1999).

Jarosite has been detected at Mars by rovers and from orbit by the Compact Reconnaissance Imaging Spectrometer for Mars (CRISM) and could play a critical role in understanding the aqueous geochemical history of Mars. Jarosite and its Al form alunite are common hydroxysulfate minerals with wide-spread occurrence on Earth (e.g., Van Breemen 1982; Desborough et al. 2010). These OH-bearing sulfates serve as indicators for salty and low pH environments, and their dissolution products provide a record of temperature, pH, and longevity of liquid water on the surface of Mars (e.g., Elwood Madden et al., 2012), where they have been observed in multiple locations (e.g., Klingelhöfer et al. 2004; Farrand et al. 2009; Weitz et al. 2011; Ehlmann et al. 2016). These minerals can form in acidic waters associated with sulfide oxidation (e.g., Burns 1987; 1988; Alpers et al. 1989; 1992; Burns 1993; Burns and Fisher 1993; Bigham et al. 1996; Herbert 1997; Crowley et al. 2003; Murad and Rojik 2003), acid sulfate soils near volcanic vents (e.g., Zimbelman et al. 2005; Schiffman et al. 2006; Bishop et al. 2007; McCollom et al. 2013; Carson et al. 2023a; 2023b) and in acidic saline lake environments (e.g., Alpers et al. 1992; Risacher et al. 2002; Benison and Laclair 2003; Baldridge et al. 2009; Story et al. 2010; Flahaut et al. 2017). Jarosite and Ca sulfates can co-exist in some environments (e.g., Elwood Madden et al. 2012; Dixon et al. 2015; Perrin et al. 2018) and a variety of iron oxides/oxyhydroxides and clays can form through jarosite dissolution (e.g., Gasharova et al. 2005; Navrotsky et al. 2005; Elwood Madden et al. 2009; 2012). Recent lab studies also demonstrate smectite formation in acidic environments (Peretyazhko et al. 2018) that supports co-formation of smectite and jarosite in our study. The presence of these accessory minerals assists in defining the geochemical history governing the formation and reaction of jarosite and alunite on Mars. A combination of jarosite and gypsum in a smectite and hydrated silica matrix is observed at the South Sulfur Bank in the banded orange/tan units and indicates low temperature hydrothermal alteration has taken place in the vicinity of volcanic vents, but not directly proximal to the vents. Similar processes may have occurred on Mars near volcanic features. The mineralogy of these banded outcrops is most similar to parts of the Noctis Labyrinthus system (Weitz et al. 2011), Gale crater (Rampe et al. 2020), and Mawrth Vallis region (Bishop et al. 2023) on Mars, where both jarosite and gypsum group minerals are observed together with smectites. Additionally, both jarosite and gypsum were identified by instruments on Opportunity at Meridiani (Squyres et al. 2006). Jarosite and a nanophase iron oxide phase were identified by the Miniature Mössbauer instrument on Opportunity (Klingelhöfer et al. 2004; Morris et al. 2004; Morris et al. 2019) and could represent altered volcanic material there.

These low-temperature hydrothermal products at the Kilauea South Sulfur Bank contain a high abundance of opal in the friable white/light colored unit and a mixture of smectites and sulfates in the orange layered outcrops. This site provides an example of the minerals formed under moderate hydrothermal conditions similar to habitable environments on Mars where biosignatures could have been preserved.

**Acknowledgments:** Support for this work at the early stages of the project from the MFR program and more recently from MDAP grant #80NSSC19K1230 is much appreciated. Thanks are also due to the National Park Service and Hawaii Volcanoes National Park for access to the site (permit #HAVO-2004-SCI-0018) and to E. Göschl for help with the field work in 2006. We thank T. Hiroi for assistance with the reflectance measurements at RELAB, Brown Univ. Emission spectra were measured at the Arizona State Univ. Mars Space Flight Facility and Mössbauer spectra were measured at Mt. Holyoke College.

**References:**

Achilles, C.N., Rampe E.B., Downs R.T., Bristow T.F., Ming D.W., Morris R.V., Vaniman D.T., Blake D.F., Yen A.S., McAdam A.C., Sutter B., Fedo C.M., Gwizd S., Thompson L.M., Gellert R., Morrison S.M., Treiman A.H., Crisp J.A., Gabriel T.S.J., Chipera S.J., Hazen R.M., Craig P.I., Thorpe M.T., Des Marais D.J., Grotzinger J.P., Tu V.M., Castle N., Downs G.W., Peretyazhko T.S., Walroth R.C., Sarrazin P., and Morookian J.M. (2020) Evidence for Multiple Diagenetic Episodes in Ancient Fluvial-Lacustrine Sedimentary Rocks in Gale Crater, Mars. Journal of Geophysical Research: Planets, 125, e2019JE006295.

Alpers, C.N., Nordstrom D.K., and Ball J.W. (1989) Solubility of jarosite solid solutions precipitated from acid mine water, Iron Mountain, California, USA. Sciences Geologiques Bulletin, 42, 281-298.

Alpers, C.N., Rye R.O., Nordstrom D.K., White L.D., and King B.-S. (1992) Chemical, crystallographic and stable isotopic properties of alunite and jarosite from acid—Hypersaline Australian lakes. Chemical Geology, 96, 203-226.

Anderson, J.H. and Wickersheim K.A. (1964) Near infrared characterization of water and hydroxyl groups on silica surfaces. Surface Science, 2, 252-260.

Baker, L.L., Nickerson R.D., and Strawn D.G. (2014) XAFS study of Fe-substituted allophane and imogolite. Clays and Clay Minerals, 62, 20-34.

Baldridge, A.M., Hook S.J., Crowley J.K., Marion G.M., Kargel J.S., Michalski J.L., Thomson B.J., de Souza Filho C.R., Bridges N.T., and Brown A.J. (2009) Contemporaneous deposition of phyllosilicates and sulfates: Using Australian acidic saline lake deposits to describe geochemical variability on Mars. Geophysical Research Letters, 36, 1-6.

Benison, K.C. and LaClair D.A. (2003) Modern and ancient extremely acid saline deposits: Terrestrial analogs for Martian environments. Astrobiology, 3, 609-618.

Benison, K.C. and Bowen B.B. (2006) Acid saline lake systems give clues about past environments and the search for life on Mars. Icarus, 183, 225-229.

Bigham, J.M., Schwertmann U., and Pfab G. (1996) Influence of pH on mineral speciation in a bioreactor simulating acid mine drainage. Applied Geochemistry, 11, 845-849.

Bishop, J.L. (2019) Chapter 4: Visible and near-infrared reflectance spectroscopy of geologic materials. In J. L. Bishop, J. F. Bell III, and J. E. Moersch, Eds., Remote Compositional Analysis: Techniques for Understanding Spectroscopy, Mineralogy, and Geochemistry of Planetary Surfaces, 68-101. Cambridge University Press. Cambridge, UK.

Bishop, J.L. and Murad E. (1996) Schwertmannite on Mars? Spectroscopic analyses of schwertmannite, its relationship to other ferric minerals, and its possible presence in the surface material on Mars. In M. D. Dyar, C. McCammon, and M. W. Schaefer, Eds., Mineral Spectroscopy: A tribute to Roger G. Burns, Special Publication Number 5, 337-358. The Geochemical Society. Houston, TX.

Bishop, J.L. and Murad E. (2005) The visible and infrared spectral properties of jarosite and alunite. American Mineralogist, 90, 1100-1107.

Bishop, J.L. and Rampe E.B. (2016) Evidence for a changing Martian climate from the mineralogy at Mawrth Vallis. Earth and Planetary Sci. Lett., 448, 42-48.

Bishop, J.L., Pieters C.M., and Edwards J.O. (1994) Infrared spectroscopic analyses on the nature of water in montmorillonite. Clays and Clay Minerals, 42, 702-716.

Bishop, J.L., Schiffman P., and Southard R.J. (2002) Geochemical and mineralogical analyses of palagonitic tuffs and altered rinds of pillow lavas on Iceland and applications to Mars. In J. L. Smellie and M. G. Chapman, Eds., Volcano-Ice Interactions on Earth and Mars, 371-392. Geological Society, Special Publication No.202. London.

Bishop, J.L., Murad E., Lane M.D., and Mancinelli R.L. (2004) Multiple techniques for mineral identification on Mars: A study of hydrothermal rocks as potential analogues for astrobiology sites on Mars. Icarus, 169, 331-323.

Bishop, J.L., Lane M.D., Dyar M.D., and Brown A.J. (2008a) Reflectance and emission spectroscopy study of four groups of phyllosilicates: Smectites, kaolinite-serpentines, chlorites and micas. Clay Minerals, 43, 35-54.

Bishop, J.L., Schiffman P., Murad E., Dyar M.D., Drief A., and Lane M.D. (2007) Characterization of Alteration Products in Tephra from Haleakala, Maui: A Visible-Infrared Spectroscopy, Mössbauer Spectroscopy, XRD, EPMA and TEM Study. Clays and Clay Minerals, 55, 1-17.

Bishop, J.L., Lane M.D., Dyar M.D., King S.J., Brown A.J., and Swayze G. (2014) Spectral properties of Ca-sulfates: Gypsum, bassanite and anhydrite. American Mineralogist, 99, 2105-2115.

Bishop, J.L., Parente M., Saranathan A.M., Gross C., Itoh Y., and Elwood Madden M.E. (2023) Diverse Phyllosilicate and Sulfate Assemblages in the Mawrth Vallis Channel. 54th Lunar Planet. Sci. Conf., The Woodlands, TX, Abstract #1913.

Bishop, J.L., Lane M.D., Dyar M.D., Parente M., Roach L.A., Murchie S.L., and Mustard J.F. (2008b) Sulfates on Mars: How recent discoveries from CRISM, OMEGA and the MERs are changing our view of the planet. Goldschmidt Conf., Vancouver, BC, abs# 18D_1678.

745 Bishop, J.L., Weitz C.M., Parente M., Gross C., Saranathan A., Itoh Y., and Al-Samir M. (2021a)
746 Correlating sulfates with the aqueous geochemical history at Juventae Chasma, Mars. 52nd
747 Lunar Planet. Sci. Conf., Virtual, Abstract #1082.
748 Bishop, J.L., Gross C., Danielsen J.M., Parente M., Murchie S.L., Horgan B., Wray J.J., Viviano
749 C.E., and Seelos F.P. (2020) Multiple mineral horizons in layered outcrops at Mawrth
750 Vallis, Mars, signify changing geochemical environments on early Mars. Icarus, 341,
751 113634.
752 Bishop, J.L., Yeşilbaş M., Hinman N.W., Burton Z. F. M., Englert P.A.J., Toner J.D., McEwen
753 A.S., Gulick V.C., Gibson E.K., and Koeberl C. (2021b) Martian subsurface cryosalt
754 expansion and collapse as trigger for landslides. Science Advances, 7, abe4459.
755 Bishop, J.L., Parente M., Weitz C.M., Noe Dobrea E.Z., Roach L.A., Murchie S.L., McGuire P.C.,
756 McKeown N.K., Rossi C.M., Brown A.J., Calvin W.M., Milliken R.E., and Mustard J.F.
757 (2009) Mineralogy of Juventae Chasma: Sulfates in the light-toned mounds, mafic minerals
758 in the bedrock, and hydrated silica and hydroxylated ferric sulfate on the plateau. Journal
759 of Geophysical Research, 114, doi:10.1029/2009JE003352.
760 Black, S.R. and Hynek B.M. (2018) Characterization of terrestrial hydrothermal alteration
761 products with Mars analog instrumentation: Implications for current and future rover
762 investigations. Icarus, 307, 235-259.
763 Bowen, B.B., Story S., Oboh-Ikuenobe F., and Benison K.C. (2013) Differences in regolith
764 weathering history at an acid and neutral saline lake on the Archean Yilgarn Craton and
765 implications for acid brine evolution. Chemical Geology, 356, 126-140.
766 Bunch, T.E. and Reid A.M. (1975) The nakhlites part 1: Petrography and mineral chemistry.
767 Meteoritics, 10, 303-315.
768 Burisch, M., Walter B.F., Gerdes A., Lanz M., and Markl G. (2018) Late-stage anhydrite-gypsum-
769 siderite-dolomite-calcite assemblages record the transition from a deep to a shallow
770 hydrothermal system in the Schwarzwald mining district, SW Germany. Geochimica et
771 Cosmochimica Acta, 223, 259-278.
772 Burns, R.G. (1987) Ferric sulfates on Mars. Journal of Geophysical Research, 92, E570-E574.
773 Burns, R.G. (1988) Gossans on Mars. Proceedings of the 18th LPSC, LPI, Houston, TX, 713-721.
774 Burns, R.G. (1993) Rates and mechanisms of chemical weathering of ferromagnesian silicate
775 minerals on Mars. Geochimica Cosmochimica Acta, 57, 4555-4574.
776 Burns, R.G. and Fisher D.S. (1993) Rates of oxidative weathering on the surface of Mars. Journal
777 of Geophysical Research, 98, 3365-3372.
778 Burton, Z.F.M., Bishop J.L., Englert P.A.J., Szynkiewicz A., Koeberl C., Dera P., Mckenzie W.,
779 and Gibson E.K. (2023) A shallow salt pond analog for aqueous alteration on ancient Mars:
780 Spectroscopy, mineralogy, and geochemistry of sediments from Antarctica's Dry Valleys
781 American Mineralogist, 108, 1017-1031.
782 Cady, S.L., Skok J.R., Gulick V.G., Berger J.A., and Hinman N.W. (2018) Chapter 7 - Siliceous
783 Hot Spring Deposits: Why They Remain Key Astrobiological Targets. In N. A. Cabrol and
784 E. A. Grin, Eds., From Habitability to Life on Mars, 179-210. Elsevier
785 Campbell, K.A., Guido D.M., Gautret P., Foucher F., Ramboz C., and Westall F. (2015) Geyserite
786 in hot-spring siliceous sinter: Window on Earth's hottest terrestrial (paleo)environment and
787 its extreme life. Earth-Science Reviews, 148, 44-64.
788 Carson, G.L., McHenry L.J., Hynek B.M., Cameron B.I., and Glenister C.T. (2023a) Mineralogy
789 and bulk geochemistry of a fumarole at Hverir, Iceland: Analog for acid-sulfate leaching
790 on Mars. American Mineralogist, 108, 409-429.

Carson, G.L., McHenry L.J., Hynek B.M., Cameron B.I., and Glenister C.T. (2023b) Mineralogy and geochemistry of hot spring deposits at Námafjall, Iceland: Analog for sulfate soils at Gusev crater, Mars. American Mineralogist, 108, 637-652.

Christensen, P.R., Bandfield J.L., Hamilton V.E., Lane M.D., Piatek J.L., Ruff S.W., and Stefanov W.L. (2000) A thermal emission spectral library of rock-forming minerals. Journal of Geophysical Research, 105, 9735-9739.

Clark, B.C. and Baird A.K. (1979) Is the Martian lithosphere sulfur rich? Journal of Geophysical Research, 84, 8395-8403.

Crowley, J.K., Williams D.E., Hammarstrom J.M., Piatak N., Chou I.-M., and Mars J.C. (2003) Spectral reflectance properties (0.4-2.5 μm) of secondary Fe-oxide, Fe-hydroxide, and Fe-sulphate-hydrate minerals associated with sulphide-bearing mine wastes. Geochemistry: Exploration, Environment, Analysis, 3, 219-228.

Desborough, G.A., Smith K.S., Lowers H.A., Swayze G.A., Hammarstrom J.M., Diehl S.F., Leinz R.W., and Driscoll R.L. (2010) Mineralogical and chemical characteristics of some natural jarosites. Geochimica et Cosmochimica Acta, 74, 1041-1056.

Dixon, E.M., Elwood Madden A.S., Hausrath E.M., and Elwood Madden M.E. (2015) Assessing hydrodynamic effects on jarosite dissolution rates, reaction products, and preservation on Mars. Journal of Geophysical Research: Planets, 120, 625-642.

Dyar, M.D. and Sklute E.C. (2019) Chapter 7: Mössbauer spectroscopy: Theory and laboratory spectra of geologic materials. In J. L. Bishop, J. F. Bell III, and J. E. Moersch, Eds., Remote Compositional Analysis: Techniques for Understanding Spectroscopy, Mineralogy, and Geochemistry of Planetary Surfaces, 147-167. Cambridge University Press. Cambridge, UK.

Dyar, M.D., Gunter M.E., and Tasa D. (2008) Mineralogy and Optical Mineralogy. 708 p. Mineralogical Society, Chantilly, VA.

Dyar, M.D., Breves E., Jawin E., Marchand G.J., Nelms M., O'Connor V., Peel S., Rothstein Y., Sklute E.C., Lane M.D., Bishop J.L., and Mertzman S.A. (2013) Mössbauer parameters of iron in sulfate minerals. American Mineralogist, 98, 1943-1965

Ehlmann, B.L., Swayze G.A., Milliken R.E., Mustard J.F., Clark R.N., Murchie S.L., Breit G.N., Wray J.J., Gondet B., Poulet F., Carter J., Calvin W.M., Benzel W.M., and Seelos K.D. (2016) Discovery of alunite in Cross crater, Terra Sirenum, Mars: Evidence for acidic, sulfurous waters. American Mineralogist, 101, 1527-1542.

Elwood Madden, M.E., Bodnar R.J., and Rimstidt J.D. (2004) Jarosite as an indicator of water-limited chemical weathering on Mars. Nature, 431, 821-823.

Elwood Madden, M.E., Madden A.S., and Rimstidt J.D. (2009) How long was Meridiani Planum wet? Applying a jarosite stopwatch to determine the duration of aqueous diagenesis. Geology, 37, 635-638.

Elwood Madden, M.E., Madden A.S., Rimstidt J.D., Zahrai S., Kendall M.R., and Miller M.A. (2012) Jarosite dissolution rates and nanoscale mineralogy. Geochimica et Cosmochimica Acta, 91, 306-321.

Farmer, J.D. (1996) Hydrothermal systems on Mars: An assessment of present evidence. In G. R. Bock and J. A. Goode, Eds., Evolution of Hydrothermal Ecocystems on Earth (and Mars?), 273-295. John Wiley & sons. New York.

Farmer, J.D. and Des Marais D.J. (1999) Exploring for a record of ancient Martian life. Journal of Geophysical Research, 104, 26,977-26,995.

Farrand, W.H., Glotch T.D., Rice J.W., Jr., Hurowitz J.A., and Swayze G.A. (2009) Discovery of jarosite within the Mawrth Vallis region of Mars: Implications for the geologic history of the region. Icarus, 204, 478-488.

Fawdon, P., Skok J.R., Balme M.R., Vye-Brown C.L., Rothery D.A., and Jordan C.J. (2015) The geological history of Nili Patera, Mars. Journal of Geophysical Research: Planets, 120, 951-977.

Flahaut, J., Martinet M., Bishop J.L., Davies G.R., and Potts N.J. (2017) Remote sensing and in situ mineralogic survey of the Chilean salars: An analog to Mars evaporate deposits? Icarus, 282, 152-173.

Flahaut, J., Bishop J.L., Silvestro S., Tedesco D., Daniel I., and Loizeau D. (2019) The Italian Solfatara as an analog for Mars fumarolic alteration. American Mineralogist, 104, 1565-1577.

Gasharova, B., Göttlicher J., and Becker U. (2005) Dissolution at the surface of jarosite: an in situ AFM study. Chemical Geology, 215, 499-516.

Geyer, C.J., Elwood Madden A.S., Rodriguez A., Bishop J.L., Mason D., and Elwood Madden M.E. (2023) The role of sulfate in cation exchange reactions: Applications to clay-brine interactions on Mars. Planetary Science Journal, 4, 48.

Gooding, J.L. (1978) Chemical weathering on Mars. Thermodynamic stabilities of primary minerals (and their alteration products) from mafic igneous rocks. Icarus, 33, 483-513.

Herbert, R.B. (1997) Properties of goethite and jarosite precipitated from acidic groundwater, Dalarna, Sweden. Clays and Clay Minerals, 45, 261-273.

Hinman, N.W., Bishop J.L., Gulick V.C., Kotler Dettmann J.M., Morkner P., Berlanga G., Henneberger R.M., Bergquist P., Richardson C.D., Walter M.R., MacKenzie L.A., Anitori R.P., and Scott J.R. (2021) Targeting mixtures of jarosite and clay minerals for Mars exploration. American Mineralogist, 106, 1237–1254.

Jensen, M.L. and Bateman A.M. (1979) Economic Mineral Deposits, 3rd ed. p. Wiley and Sons, New York.

Johnson, J.R., Bell J.F., III, Cloutis E.A., Staid M.I., Farrand W.H., McCoy T., Rice M., Wang A., and Yen A.S. (2007) Mineralogic constraints on sulfur-rich soils from Pancam spectra at Gusev Crater, Mars. Geophysical Research Letters, 34, L13202, doi:10.1029/2007GL029894.

Jones, B. (2021) Siliceous sinters in thermal spring systems: Review of their mineralogy, diagenesis, and fabrics. Sedimentary Geology, 413, 105820.

Klingelhöfer, G., Morris R.V., Bernhardt B., Schröder C., Rodionov D., de Souza P.A.J., Yen A.S., Gellert R., Evlanov E.N., Zubkov B., Foh J., Bonnes U., Kankeleit E., Gütlich P., Ming D.W., Renz F., Wdowiak T.J., Squyres S.W., and Arvidson R.E. (2004) Jarosite and hematite at Meridiani Planum from Opportunity's Mössbauer spectrometer. Science, 306, 1740-1745.

Lane, M.D. and Christensen P.R. (1998) Thermal infrared emission spectroscopy of salt minerals predicted for Mars. Icarus, 135, 528-536.

Lane, M.D. and Bishop J.L. (2019) Chapter 3: Mid-infrared (thermal) emission and reflectance spectroscopy. In J. L. Bishop, J. F. Bell III, and J. E. Moersch, Eds., Remote Compositional Analysis: Techniques for Understanding Spectroscopy, Mineralogy, and Geochemistry of Planetary Surfaces, 42-67. Cambridge University Press. Cambridge, UK.

Lane, M.D., Bishop J.L., Dyar M.D., King P.L., Parente M., and Hyde B.C. (2008) Mineralogy of the Paso Robles Soils on Mars. American Mineralogist, 93, 728-739.

McCollom, T.M., Hynek B.M., Rogers K., Moskowitz B., and Berquó T.S. (2013) Chemical and mineralogical trends during acid-sulfate alteration of pyroclastic basalt at Cerro Negro volcano and implications for early Mars. Journal of Geophysical Research: Planets, 118, 1719-1751.

McCubbin, F.M., Tosca N.J., Smirnov A., Nekvasil H., Steele A., Fries M., and Lindsley D.H. (2009) Hydrothermal jarosite and hematite in a pyroxene-hosted melt inclusion in martian meteorite Miller Range (MIL) 03346: Implications for magmatic-hydrothermal fluids on Mars. Geochimica et Cosmochimica Acta, 73, 4907-4917.

McSween, H.Y., Jr. (1994) What have we learned about Mars from SNC meteorites. Meteoritics, 29, 757-779.

McSween, H.Y., Jr. (2002) The rocks of Mars, from far and near. Meteoritics and Planetary Science, 37, 7-25.

Moore, R.D. and Szynkiewicz A. (2023) Aqueous sulfate contributions in terrestrial basaltic catchments: Implications for understanding sulfate sources and transport in Meridiani Planum, Mars. Icarus, 391, 115342.

Morris, R.V., Schröder C., Klingelhöfer G., and Agresti D.G. (2019) Chapter 27: Mössbauer spectroscopy of Gusev crate and Meridiani Planum. In J. L. Bishop, J. F. Bell III, and J. E. Moersch, Eds., Remote Compositional Analysis: Techniques for Understanding Spectroscopy, Mineralogy, and Geochemistry of Planetary Surfaces, 538-553. Cambridge University Press. Cambridge, UK.

Morris, R.V., Lauer Jr. H.V., Lawson C.A., Gibson Jr. E.K., Nace G.A., and Stewart C. (1985) Spectral and other physicochemical properties of submicron powders of hematite (a-$Fe_2O_3$), maghemite (g-$Fe_2O_3$), magnetite ($Fe_3O_4$), goethite (a-FeOOH), and lepidocrocite (g-FeOOH). Journal of Geophysical Research, 90, 3126-3144.

Morris, R.V., Agresti D.G., Lauer Jr. H.V., Newcomb J.A., Shelfer T.D., and Murali A.V. (1989) Evidence for pigmentary hematite on Mars based on optical, magnetic and Mössbauer studies of superparamagnetic (nanocrystalline) hematite. Journal of Geophysical Research, 94, 2760-2778.

Morris, R.V., Graff T., Lane M.D., Golden D.C., Schwandt C.S., Shelfer T.D., Ming D.W., Mertzman S.A., Bell III J.F., Crisp J.A., and Christensen P.R. (2000) Acid sulfate alteration products of a tholeiitic basalt: Implications for interpretation of martian thermal emission spectra. Lunar Planet. Sci. XXXI., Lunar Planet. Inst., Houston., CD-ROM #2014 (abstr.).

Morris, R.V., Klingelhöfer G., Bernhardt B., Schröder C., Rodionov D.S., de Souza P.A., Jr., Yen A.S., Gellert R., Evlanov E.N., Foh J., Kankeleit E., Güttlich P., Ming D.W., Renz F., Wdowiak T.J., Squyres S.W., and Arvidson R.E. (2004) Mineralogy at Gusev Crater from the Mössbauer Spectrometer on the Spirit Rover. Science, 305, 833-836.

Murad, E. and Schwertmann U. (1980) The Mössbauer spectrum of ferrihydrite and its relations to those of the other iron oxides. American Mineralogist, 65, 1044-1049.

Murad, E. and Rojik P. (2003) Iron-rich precipitates in a mine drainage environment: Influence of pH on mineralogy. American Mineralogist, 88, 1915-1918.

Murchie, S.L., Mustard J.F., Ehlmann B.L., Milliken R.E., Bishop J.L., McKeown N.K., Noe Dobrea E.Z., Seelos F.P., Buczkowski D.L., Wiseman S.M., Arvidson R.E., Wray J.J., Swayze G.A., Clark R.N., Des Marais D.J., McEwen A.S., and Bibring J.P. (2009) A synthesis of Martian aqueous mineralogy after one Mars year of observations from the Mars Reconnaissance Orbiter. Journal of Geophysical Research, 114, E00D06, doi:10.1029/2009JE003342.

Navrotsky, A., Forray F.L., and Drouet C. (2005) Jarosite stability on Mars. Icarus, 176, 250-253.

Parente, M., Bishop J.L., and Bell J.F. (2009) Spectral unmixing for mineral identification in Pancam images of soils in Gusev Crater, Mars. Icarus, 203, 421-436.

Peretyazhko, T.S., Niles P.B., Sutter B., Morris R.V., Agresti D.G., Le L., and Ming D.W. (2018) Smectite formation in the presence of sulfuric acid: Implications for acidic smectite formation on early Mars. Geochimica et Cosmochimica Acta, 220, 248-260.

Perrin, S., Bishop J.L., Parker W.G., King S.J., and Lafuente B. (2018) Mars evaporite analog site containing jarosite and gypsum at Sulfate Hill, Painted Desert, AZ. 49th Lunar Planet. Sci. Conf., The Woodlands, TX, Abstract #1801.

Rampe, E.B., Blake D.F., Bristow T.F., Ming D.W., Vaniman D.T., Morris R.V., Achilles C.N., Chipera S.J., Morrison S.M., Tu V.M., Yen A.S., Castle N., Downs G.W., Downs R.T., Grotzinger J.P., Hazen R.M., Treiman A.H., Peretyazhko T.S., Des Marais D.J., Walroth R.C., Craig P.I., Crisp J.A., Lafuente B., Morookian J.M., Sarrazin P.C., Thorpe M.T., Bridges J.C., Edgar L.A., Fedo C.M., Freissinet C., Gellert R., Mahaffy P.R., Newsom H.E., Johnson J.R., Kah L.C., Siebach K.L., Schieber J., Sun V.Z., Vasavada A.R., Wellington D., and Wiens R.C. (2020) Mineralogy and geochemistry of sedimentary rocks and eolian sediments in Gale crater, Mars: A review after six Earth years of exploration with Curiosity. Geochemistry, 80, 125665.

Rapin, W., Chauviré B., Gabriel T.S.J., McAdam A.C., Ehlmann B.L., Hardgrove C., Meslin P.Y., Rondeau B., Dehouck E., Franz H.B., Mangold N., Chipera S.J., Wiens R.C., Frydenvang J., and Schröder S. (2018) In Situ Analysis of Opal in Gale Crater, Mars. Journal of Geophysical Research: Planets, 123, 1955-1972.

Rice, M.S., Bell III J.F., Cloutis E.A., Wang A., Ruff S.W., Craig M.A., Bailey D.T., Johnson J.R., de Souza Jr. P.A., and Farrand W.H. (2010) Silica-rich deposits and hydrated minerals at Gusev Crater, Mars: Vis-NIR spectral characterization and regional mapping. Icarus, 205, 375-395.

Risacher, F., Alonso H., and Salazar C. (2002) Hydrochemistry of two adjacent acid saline lakes in the Andes of northern Chile. Chemical Geology, 187, 39-57.

Roach, L.H., Mustard J.F., Swayze G.A., Milliken R., Bishop J.L., Murchie S.L., and Lichtenberg K.A. (2010) Hydrated mineral stratigraphy of Ius Chasma, Valles Marineris. Icarus, 206, 253-268.

Ruff, S.W. and Farmer J.D. (2016) Silica deposits on Mars with features resembling hot spring biosignatures at El Tatio in Chile. Nature Communications, 7, 13554.

Ruff, S.W., Farmer J.D., Calvin W.M., Herkenhoff K.E., Johnson J.R., Morris R.V., Rice M.S., Arvidson R.E., Bell Iii J.F., Christensen P.R., and Squyres S.W. (2011) Characteristics, distribution, origin, and significance of opaline silica observed by the Spirit rover in Gusev crater, Mars. Journal of Geophysical Research: Planets, 116.

Schiffman, P., Spero H.J., Southard R.J., and Swanson D.A. (2000) Controls on palagonitization versus pedogenic weathering of basaltic tephra: Evidence from the consolidation and geochemistry of the Keanakako'i ash member, Kilauea volcano. Geochemistry Geophysics Geosystems, 1, Paper no. 2000GC000068.

Schiffman, P., Southard R.J., Eberl D.D., and Bishop J.L. (2002) Distinguishing palagonitized from pedogenically-altered basaltic Hawaiian tephra: mineralogical and geochemical criteria. In J. L. Smellie and M. G. Chapman, Eds., Volcano-Ice Interactions on Earth and Mars, 393-405. Geological Society, Special Publication No.202. London.

973 Schiffman, P., Zierenberg R.A., Marks N., Bishop J.L., and Dyar M.D. (2006) Acid fog deposition
974 at Kilauea Volcano: A possible mechanism for the formation of siliceous-sulfate rock
975 coatings on Mars. Geology, 34, 921-924; doi: 10.1130/G22620A.1.
976 Schulze-Makuch, D., Dohm J.M., Fan C., Fairén A.G., Rodriguez J.A.P., Baker V.R., and Fink
977 W. (2007) Exploration of hydrothermal targets on Mars Icarus, 189, 308-324.
978 Seelos, K.D., Arvidson R.E., Jolliff B.L., Chemtob S.M., Morris R.V., Ming D.W., and Swayze
979 G.A. (2010) Silica in a Mars analog environment: Ka'u Desert, Kilauea Volcano, Hawaii.
980 Journal of Geophysical Research: Planets, 115, doi:10.1029/2009JE003347.
981 Skok, J.R., Mustard J.F., Ehlmann B.L., Milliken R.E., and Murchie S.L. (2010) Silica deposits in
982 the Nili Patera caldera on the Syrtis Major volcanic complex on Mars. Nature Geoscience,
983 3, doi: 10.1038/NGEO990.
984 Squyres, S.W., Aharonson O., Clark B.C., Cohen B.A., Crumpler L., DeSouza P.A., Farrand W.H.,
985 Gellert R., Grant J., Grotzinger J.P., Haldemann A.F.C., Johnson J.R., Klingelhöfer G.,
986 Lewis K.W., Li R., McCoy T., McEwen A.S., McSween H.Y., Ming D.W., Moore J.M.,
987 Morris R.V., Parker T.J., Rice J.W., Jr., Ruff S., Schmidt M., Schröder C., Soderblom L.A.,
988 and Yen A. (2007) Pyroclastic Activity at Home Plate in Gusev Crater, Mars. Science, 316,
989 738-742.
990 Squyres, S.W., Arvidson R.E., Bollen D., Bell III J.F., Brückner J., Cabrol N.A., Calvin W.M.,
991 Carr M.H., Christensen P.R., Clark B.C., Crumpler L., Des Marais D.J., d'Uston C.,
992 Economou T., Farmer J., Farrand W.H., Folkner W., Gellert R., Glotch T.D., Golombek
993 M., Gorevan S., Grant J.A., Greeley R., Grotzinger J., Herkenhoff K.E., Hviid S., Johnson
994 J.R., Klingelhöfer G., Knoll A.H., Landis G., Lemmon M., Li R., Madsen M.B., Malin
995 M.C., McLennan S.M., McSween H.Y., Ming D.W., Moersch J., Morris R.V., Parker T.,
996 Rice Jr. J.W., Richter L., Rieder R., Schroder C., Sims M., Smith M., Smith P., Soderblom
997 L.A., Sullivan R., Tosca N.J., Wänke H., Wdowiak T., Wolff M., and Yen A. (2006)
998 Overview of the Opportunity Mars Exploration Rover Mission to Meridiani Planum: Eagle
999 Crater to Purgatory Ripple. Journal of Geophysical Research, 111,
1000 doi:10.1029/2006JE002771.
1001 Story, S., Bowen B.B., Benison K.C., and Schulze D.G. (2010) Authigenic phyllosilicates in
1002 modern acid saline lake sediments and implications for Mars. Journal of Geophysical
1003 Research: Planets, 115, doi:10.1029/2010JE003687.
1004 Thollot, P., Mangold N., Ansan V., Le Mouélic S., Milliken R.E., Bishop J.L., Weitz C.M., Roach
1005 L.H., Mustard J.F., and Murchie S.L. (2012) Most Mars minerals in a nutshell: Various
1006 alteration phases formed in a single environment in Noctis Labyrinthus. Journal of
1007 Geophysical Research, 117, E00J06, doi: 10.1029/2011je004028.
1008 Toulmin III, P., Baird A.K., Clark B.C., Keil K., Rose J.H.J., Christian R.P., Evans P.H., and
1009 Kelliher W.C. (1977) Geochemical and mineralogial interpretation of the Viking inorganic
1010 chemical results. Journal of Geophysical Research, 82, 4625-4634.
1011 Usabal, G.S. and Bishop J.L. (2018) VNIR spectral analysis of laboratory nontronite/jarosite
1012 mixtures: Applications to Mawrth Vallis. AGU Fall Meeting, Washington, DC, Abstract
1013 #P31H-3806.
1014 Van Breemen, N. (1982) Genesis, Morphology, and Classification of Acid Sulfate Soils in Coastal
1015 PlainsEds., Acid Sulfate Weathering, 95-108
1016 Vaniman, D., Martínez G.M., Rampe E.B., Bristow T.F., Blake D., Yen A., Ming D., Rapin W.,
1017 Meslin P., Morookian J., Downs R.T., Chipera S.J., Morris R.V., Morrison S.M., Treiman
1018 A.H., Achilles C.H., Roberston K., Grotzinger J.P., Hazen R.M., Wiens R.C., and Sumner

1019 D.Y. (2018) Gypsum, bassanite, and anhydrite at Gale crater, Mars. American
1020 Mineralogist, 103, 1011-1020.
1021 Walter, M.R. and Des Marais D.J. (1993) Preservation of biological information in thermal spring
1022 deposits: Developing a strategy for the search for fossil life on Mars. Icarus, 101, 129-143.
1023 Warren-Rhodes, K., Cabrol N.A., Phillips M., Tebes-Cayo C., Kalaitzis F., Ayma D., Demergasso
1024 C., Chong-Diaz G., Lee K., Hinman N., Rhodes K.L., Boyle L.N., Bishop J.L., Hofmann
1025 M.H., Hutchinson N., Javiera C., Moersch J., Mondro C., Nofke N., Parro V., Rodriguez
1026 C., Sobron P., Sarazzin P., Wettergreen D., Zacny K., and the S.I.N.A.I.T. (2023) Orbit-
1027 to-ground framework to decode and predict biosignature patterns in terrestrial analogues.
1028 Nature Astronomy, 7, 406-422.
1029 Weitz, C.M., Bishop J.L., and Grant J.A. (2013) Gypsum, opal, and fluvial channels within a
1030 trough of Noctis Labyrinthus, Mars: Implications for aqueous activity during the Late
1031 Hesperian to Early Amazonian. Planet. Space Sci, 87, 130-145.
1032 Weitz, C.M., Bishop J.L., Thollot P., Mangold N., and Roach L.H. (2011) Diverse mineralogies
1033 in two troughs of Noctis Labyrinthus, Mars. Geology, 39, 899-902, doi:
1034 10.1130/G32045.1.
1035 Wolfe, E.W. and Morris J. (1996) Geologic map of the Island of Hawaii, 18. p. U.S. Geological
1036 Survey
1037 Yant, M., Young K.E., Rogers A.D., McAdam A.C., Bleacher J.E., Bishop J.L., and Mertzman
1038 S.A. (2017) Visible, Near-Infrared and Mid-Infrared Spectral Characterization of Hawaiian
1039 Fumarolic Alteration near Kilauea's December 1974 Flow: Implications for Spectral
1040 Discrimination of Alteration Environments on Mars. American Mineralogist, 103, 11-25.
1041 Yen, A.S., Morris R.V., Clark B.C., Gellert R., Knudson A.T., Squyres S., Mittlefehldt D.W.,
1042 Ming D.W., Arvidson R., Mccoy T., Schmidt M., Hurowitz J., Li R., and Johnson J.R.
1043 (2008) Hydrothermal processes at Gusev Crater: An evaluation of Paso Robles class soils.
1044 Journal of Geophysical Research, 113, E06S10, doi:10.1029/2007JE002978.
1045 Zimbelman, D.R., Rye R.O., and Breit G.N. (2005) Origin of secondary sulfate minerals on active
1046 andesitic stratovolcanoes. Chemical Geology, 215, 37-60.

1047